

Structure of the OMEGA nickase IsrB in complex with ω RNA and target DNA

<https://doi.org/10.1038/s41586-022-05324-6>

Received: 20 April 2022

Accepted: 6 September 2022

Published online: 12 October 2022

Open access

 Check for updates

Seiichi Hirano^{1,2,3,4,5,8}, Kalli Kappel^{1,2,3,4,5,8}, Han Altae-Tran^{1,2,3,4,5}, Guilhem Faure^{1,2,3,4,5}, Max E. Wilkinson^{1,2,3,4,5}, Soumya Kannan^{1,2,3,4,5}, F. Esra Demircioglu^{1,2,3,4,5}, Rui Yan⁶, Momoko Shiozaki⁶, Zhiheng Yu⁶, Kira S. Makarova⁷, Eugene V. Koonin⁷, Rhianon K. Macrae^{1,2,3,4,5} & Feng Zhang^{1,2,3,4,5}✉

RNA-guided systems, such as CRISPR–Cas, combine programmable substrate recognition with enzymatic function, a combination that has been used advantageously to develop powerful molecular technologies^{1,2}. Structural studies of these systems have illuminated how the RNA and protein jointly recognize and cleave their substrates, guiding rational engineering for further technology development³. Recent work identified a new class of RNA-guided systems, termed OMEGA, which include IscB, the likely ancestor of Cas9, and the nickase IsrB, a homologue of IscB lacking the HNH nuclease domain⁴. IsrB consists of only around 350 amino acids, but its small size is counterbalanced by a relatively large RNA guide (roughly 300-nt ω RNA). Here, we report the cryogenic-electron microscopy structure of *Desulfovibrio thermocuniculi* IsrB (DtIsrB) in complex with its cognate ω RNA and a target DNA. We find the overall structure of the IsrB protein shares a common scaffold with Cas9. In contrast to Cas9, however, which uses a recognition (REC) lobe to facilitate target selection, IsrB relies on its ω RNA, part of which forms an intricate ternary structure positioned analogously to REC. Structural analyses of IsrB and its ω RNA as well as comparisons to other RNA-guided systems highlight the functional interplay between protein and RNA, advancing our understanding of the biology and evolution of these diverse systems.

The RNA-guided IsrB protein is an OMEGA family member encoded in the IS200/IS605 superfamily of transposons. IsrB is the likely antecedent of IscB, another OMEGA family member that is the apparent ancestor of Cas9, as indicated both by phylogenetic analysis and by the shared unique domain architecture^{4,5}. Like IscB and Cas9, IsrB contains a RuvC-like nuclease domain that is interrupted by the insertion of a bridge helix (BH) (Fig. 1a). However, in contrast to IscB and Cas9, IsrB lacks the HNH nuclease domain, the REC lobe and large portions of the protospacer adjacent motif- (PAM-)interacting domain and, accordingly, is much smaller (at roughly 350 amino acids) than Cas9. IsrB additionally contains an N-terminal PLMP domain (named after its conserved amino acid motif) and an uncharacterized C-terminal domain (Fig. 1b). Previous work has shown that IsrB associates with a roughly 300-nt ω RNA, which guides IsrB to nick the non-target strand of double-stranded (ds) DNA containing a 5'-NTGA-3' target-adjacent motif (TAM)⁴.

Structure of the IsrB– ω RNA–target DNA complex

To characterize the molecular mechanism of ω RNA-guided DNA targeting by IsrB, we analysed a ternary complex comprising *Desulfovibrio thermocuniculi* IsrB (DtIsrB), a 284-nt ω RNA containing a 20-nt guide

segment, a 31-nt target DNA strand and a 10-nt non-target DNA strand using single-particle cryo-EM (Fig. 1c). We obtained a three-dimensional (3D) reconstruction of the ternary complex with an overall resolution of 3.1 Å (Fig. 1d, Extended Data Fig. 1a–c and Extended Data Table 1). Some regions of the map corresponding to the ω RNA, however, were resolved at a lower resolution. To refine the modelling of the RNA coordinates, we used an RNA-specific modelling tool, auto-DRRAFTER, together with a covariance-based secondary structure model to build an initial ω RNA model. On the basis of this ω RNA model and an initial IsrB model generated by protein structure prediction, we determined the IsrB– ω RNA–DNA structure (Fig. 1e and Extended Data Figs. 1d,e and 2)^{6–8}.

The structure revealed that IsrB extensively binds to target DNA through a 20-nt duplex between the ω RNA and target DNA (Fig. 1e). The RuvC domain (residues 60–253) encompasses the three catalytic motifs (RuvC I–III) and three insertions (BH (residues 92–112), A (residues 113–129) and B (residues 161–179)) (Fig. 1b). Insertion A is a ‘shortcut’ linker between BH and RuvC II; this linker is replaced with the REC lobe in Cas9. Thus, we denote this insertion the REC linker (RECL). Insertion B, between RuvC II and III, is a simple linker consisting of a loop and an α helix that in the IsrB structure occupies a position corresponding to that of the HNH domain in Cas9. Thus, we denote it the HNH linker (HNHL). The C-terminal domain (residues 287–351) adopts a core fold

¹Broad Institute of MIT and Harvard, Cambridge, MA, USA. ²McGovern Institute for Brain Research at MIT, Cambridge, MA, USA. ³Department of Brain and Cognitive Science, Massachusetts Institute of Technology, Cambridge, MA, USA. ⁴Department of Biological Engineering, Massachusetts Institute of Technology, Cambridge, MA, USA. ⁵Howard Hughes Medical Institute, Cambridge, MA, USA. ⁶CryoEM Shared Resources, Howard Hughes Medical Institute, Janelia Research Campus, Ashburn, VA, USA. ⁷National Center for Biotechnology Information, National Library of Medicine, National Institutes of Health, Bethesda, MD, USA. ⁸These authors contributed equally: Seiichi Hirano, Kalli Kappel. ✉e-mail: zhang@broadinstitute.org

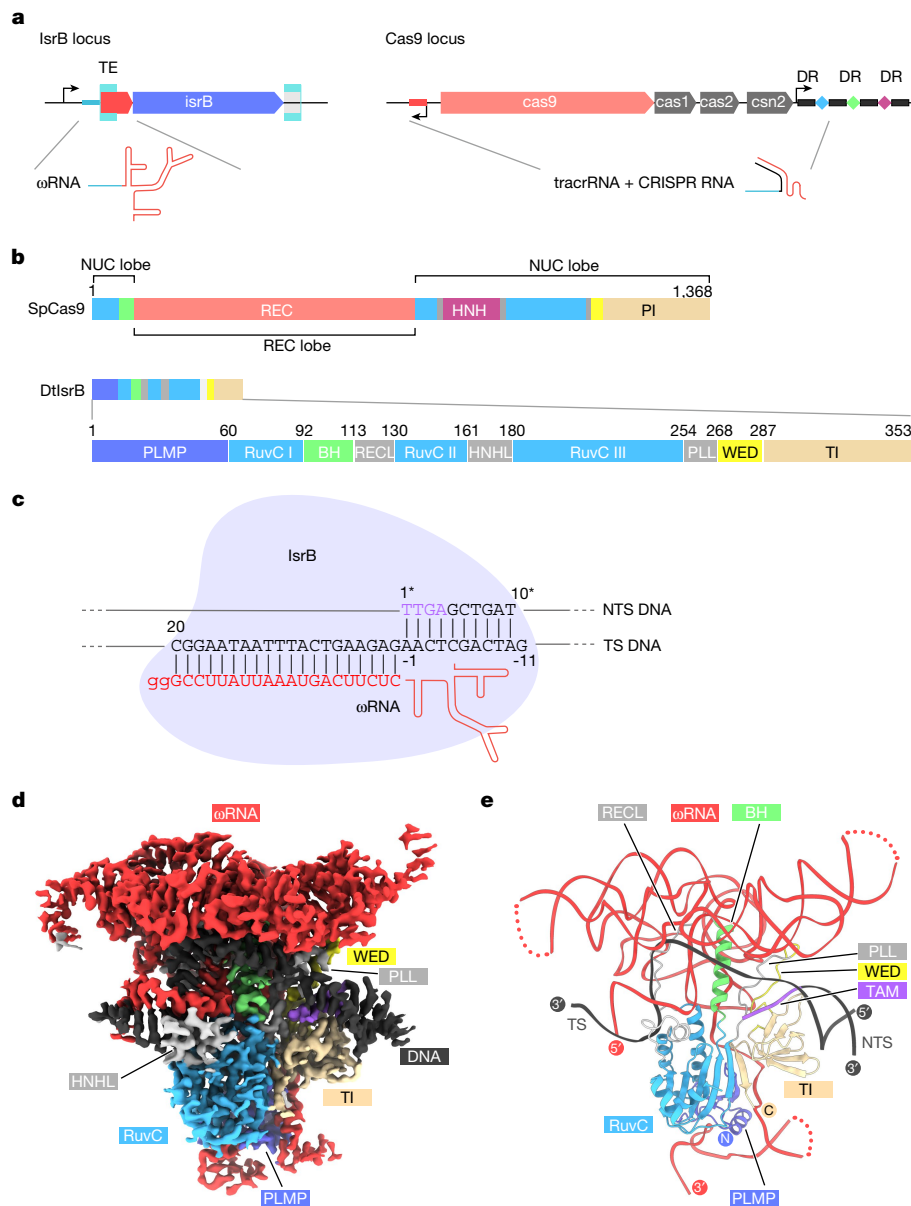


Fig. 1 | Cryogenic-electron microscopy (cryo-EM) structure of the IsrB- ω RNA-target DNA complex. **a**, Locus architecture and guide RNAs for IsrB (left) and Cas9 (right). **b**, Domain architecture of *Streptococcus pyogenes* SpCas9 (top) and *D. thermocuniculi* IsrB (DtlIsrB) (bottom). **c**, Schematic of IsrB in complex with the ω RNA and the target DNA. The partial DNA duplex containing the TAM and target sequences used for the structural study are

shown in sequence letters. **d, e**, Cryo-EM-density map (**d**) and structural model (**e**) of the IsrB- ω RNA-target DNA complex. Dashed lines represent poorly resolved regions of ω RNA. TE, transposon end; DR, direct repeat; NUC, nuclease; PI, PAM-interacting; PLL, phosphate-lock loop; TI, TAM-interacting; TS, target strand; NTS, non-target strand.

comprising two distorted β sheets (β 1/2/6 and β 3/4/5) and binds to the TAM-containing DNA duplex (Fig. 1e and Extended Data Fig. 3a). We denote this domain as the TAM-interacting (TI) domain because of structural and functional similarities to the PAM-interacting domain of Cas9 (Extended Data Fig. 3b). The extra β strand (β 7) extensively interacts with the core fold of the TI domain and shares a common β sheet with the RuvC core that adopts the RNaseH fold (Extended Data Fig. 3a). This arrangement suggests that the TI and RuvC domains cooperate to define the distance between the RuvC active site and the TAM-binding site (Fig. 1e). The intermediate regions A (residues 254–267) and B (268–286) between the RuvC and TI domains seem to be functionally analogous to the phosphate-lock loop and WED domain of Cas9, respectively, and we therefore adopted those terms for IsrB (Fig. 1e). The PLMP domain (residues 1–59) features a four-stranded, antiparallel

β sheet (β 1–4) and an α helix, and is structurally similar to the N-terminal domain of translation initiation factor 3 (Fig. 1e and Extended Data Figs. 3a and 4). In this domain, the PLMP motif-containing strand (β 2) is bulged due to two prolines (Pro17 and Pro20) disrupting one of the hydrogen bonds, but seems to keep the integrity of a coherent strand (β 1). The PLMP domain extensively interacts with the RuvC and TI domains, suggesting a role in supporting their functions.

ω RNA architecture

The ω RNA consists of the 20-nt guide segment, which base pairs with the target DNA, and the 262-nt ω RNA scaffold. This scaffold consists of 12 helices (four stems (S1–4) and eight stem loops (SL1–8)), which are located on three layers (layer 1, S1/3 and SL1/2/5/6; layer 2, S2/4

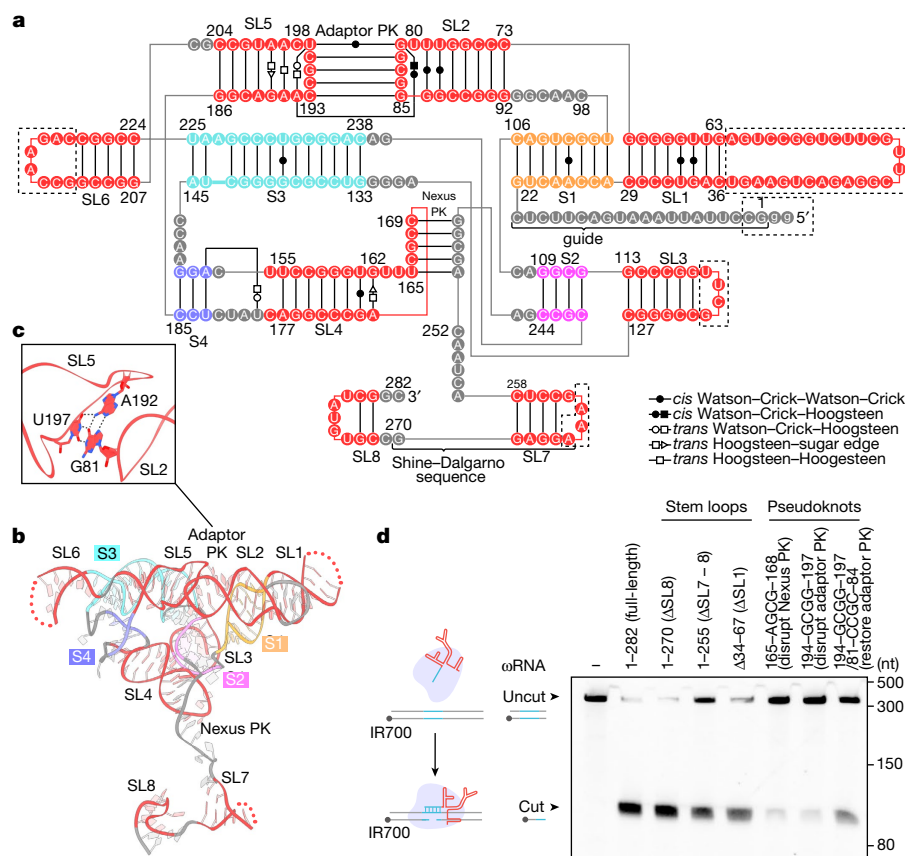


Fig. 2 | Model of the DtlrB ω RNA structure. **a, b**, Schematic (**a**) and structural model (**b**) of the ω RNA scaffold (residues 21–282). S1–4, stem 1–4; SL1–8, stem loop 1–8; PK, pseudoknot. In **a**, canonical and non-canonical base pairs are depicted by solid black lines. Poorly resolved regions are enclosed in a dashed box. In **b**, the guide segment is omitted for clarity. **c**, A base-triple formation in the adaptor pseudoknot. Hydrogen bonds are shown as dashed lines. **d**, In vitro reconstituted DtlrB- ω RNA RNP nicking of dsDNA substrates (with TTGA TAM)

and SL3/4; layer3, SL7/8) (Fig. 2a,b). All the RNA helices are packed together by various RNA interactions. The S1-SL1, S2-SL3 and S3-SL6 combinations are directly stacked in each combination. S4 and SL4 are co-axially stacked due to the direct stack between A152 and U154 and the base-triple formation among A152, U179 and U183. SL2 and SL5 form a pseudoknot (which we denote as the adaptor pseudoknot), which is capped by a base-triple formed by G81, A192 and U197 (Fig. 2c). Some RNA helices connect layers within the globular ω RNA structure. S2, C107, A108, G245 and A246 form the nexus region, which is widely conserved in the tracrRNA of Cas9s (ref. ⁹) (Fig. 2a). This nexus region and S4 are directly connected to S1 and SL5, respectively, between layers 1 and 2. SL4 forms a pseudoknot (which we denote as the nexus pseudoknot) with the region between S2 and SL7, enabling interactions between layers 2 and 3 (Fig. 2a,b). Mutations disrupting base pairs in the pseudoknots abolished the DNA nicking activity, and subsequent mutations restoring base pairs in the adaptor pseudoknot partially restored this activity, highlighting the importance of the pseudoknots for ω RNA function (Fig. 2d). These structural and biochemical data show that the ω RNA forms a compact, globular structure achieved by various RNA interactions. Such a structure may be beneficial for OMEGA systems: if the ω RNA autonomously forms its globular structure and functions as a scaffold (in contrast to tracrRNA), the effector protein does not need auxiliary motifs/domains to support RNA folding and function. Furthermore, if the globular shape provides some resistance to endogenous RNA degradation, it could facilitate ω RNA functioning in *trans* with an effector protein. This latter possibility is supported by

with full-length ω RNA or truncated ω RNA. $n = 3$ independent technical replicates. $\Delta 34-67$, ω RNA in which nucleotides 34–67 were replaced with GAAA; 165-AGCG-168, ω RNA in which nucleotides 165–168 were replaced with AGCG; 194-GCGG-197, ω RNA in which nucleotides 194–197 were replaced with CCGG; 194-GCGG-197/81-CCGC-84, ω RNA in which nucleotides 81–84 and 194–197 were replaced with CCGC and GCGG, respectively.

the finding of standalone ω RNAs that can function with the related OMEGA effector IscB⁴.

The 5'-stem region of ω RNA (S1, SL1 and SL2) is designated the guide adaptor region. It seems that during the evolutionary transition from OMEGA system to CRISPR-Cas, SL2 and the descending strands of S1/SL1 of the ω RNA were adapted to form the CRISPR array to enable the formation of the functional Cas9-CRISPR RNA (crRNA)-tracrRNA complex (Fig. 1a). The genomic sequence encoding the guide adaptor region is important for IS200/IS605 transposon activity in bacterial genomes¹⁰ (Fig. 2a). We truncated part of this region, SL1 (Δ SL1 ω RNA), and found that the resulting RNA still supported robust DNA nicking activity by IsrB (Fig. 2d). Furthermore, we reconstituted Δ SL1 ω RNA with the IsrB protein and target DNA and performed a single-particle analysis, generating a 6.9-Å resolution map (Extended Data Fig. 6a–e). Comparing this map with that of the full-length RNA validated the SL1 position determined from our RNA model and revealed conformational similarity between the full-length and Δ SL1 RNAs (Extended Data Fig. 6a,b). These results indicate that SL1 in the guide adaptor region is not required for target DNA nicking by IsrB and instead may contribute to other functions involved in the mobility of IsrB-encoding transposons. The ω RNA scaffold extensively interacts with all parts of IsrB except for the HNHL region (Fig. 1e). In particular, the PLMP domain interacts with the tandem hairpins (SL7 and SL8) near the 3' end of the ω RNA. The truncation of SL7/8, but not SL8 reduced the nicking activity of IsrB (Fig. 2d). Given that the terminal hairpin (SL7) of the ω RNA contains the Shine-Dalgarno sequence located immediately upstream

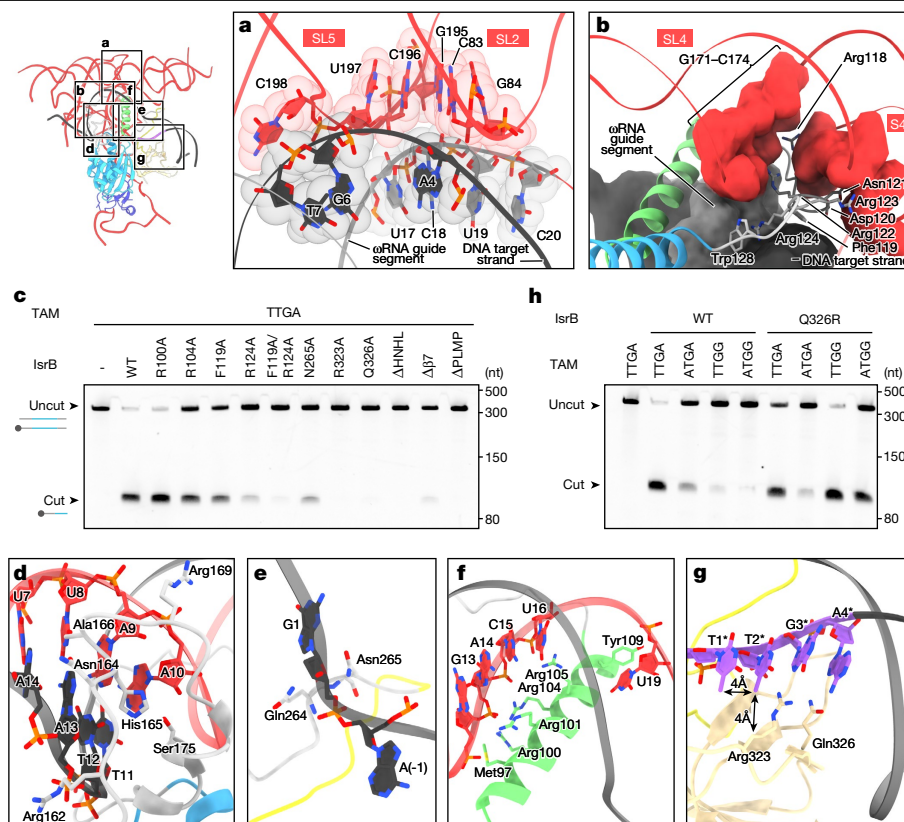


Fig. 3 | DNA targeting and nicking mechanism of IsrB. Inset shows the location of zoomed in panels. **a**, Heteroduplex recognition by the adaptor pseudoknot. **b**, Heteroduplex recognition by SL4, S4 and RECL. The volumes of RNA and DNA are generated from atomic coordinates, using Chimera X. **c**, In vitro reconstituted DtlSrB- ω RNA RNP nicking of dsDNA substrates (with TTGA TAM) with wild-type (WT) or mutant DtlSrB. $n = 3$ independent technical replicates. Δ HNHL, IsrB mutant in which residues 161–174 were replaced with a GSG-linker. $\Delta\beta 7$, IsrB mutant in which residues 341–353 were deleted. Δ PLMP, IsrB mutant in which residues 1–52 were deleted. To confirm the protein

stability of deletion mutants, we checked the protein expression in bacterial lysate overexpressing the deletion mutants (Extended Data Fig. 5b).

d, Heteroduplex recognition by HNHL. **e**, Recognition of the +1 phosphate (phosphodiester bond between nucleotides dG1 and dA(-1) of target strand DNA) by the phosphate-lock loop. **f**, Recognition of the guide segment by BH. **g**, TAM recognition by the TI domain. **h**, TAM specificity of DtlSrB. In vitro reconstituted DtlSrB- ω RNA RNP nicking of dsDNA substrates (with TTGA/ATGA/TTGG/ATGG TAMs) with WT or mutant DtlSrB. $n = 3$ independent technical replicates.

of the IsrB-coding region, these results indicate that the IsrB- ω RNA interaction is important for IsrB function and could contribute to the regulation of IsrB expression in its native context.

DNA-targeting mechanism of IsrB- ω RNA complex

We next sought to leverage structural information to decipher the DNA-targeting mechanism of IsrB. The gRNA-target DNA heteroduplex is surrounded by S2/S3/S4/SL2/SL4/SL5 of the ω RNA as well as the RuvC domain and the BH/RECL/HNHL regions of IsrB (Figs. 1e and 2b). SL2, SL4 and SL5 directly contact the heteroduplex backbone through hydrogen bonds and van der Waals interactions (Fig. 3a,b). S2, S3 and S4 indirectly recognize the heteroduplex backbone, using a short peptide linker, RECL, in which residues 113–124 are induced to fit into the grooves of S2/S3/S4 and the heteroduplex (Fig. 3b)¹¹. Mutating F119 and R124 to alanine reduced the DNA nicking activity of IsrB, highlighting the functional importance of these residues in the RECL (Fig. 3c). In addition to the ω RNA, the IsrB protein binds extensively to the heteroduplex (Fig. 1e). The HNHL recognizes the minor groove of the heteroduplex through interactions with the backbone ribose moieties (Fig. 3d). We confirmed the importance of this interaction by deleting residues V161–F174 in the HNHL, which abolished the DNA nicking activity (Fig. 3c and Extended Data Fig. 5b). Several arginine residues in the BH contact the phosphate backbone of the ω RNA guide segment in a similar manner to that in the Cas9-guide RNA complex, in which

the guide RNA-BH interactions pre-order the guide region for DNA recognition and unwinding¹² (Fig. 3f). Mutating R104, but not R100, to alanine reduced the DNA nicking activity of IsrB, highlighting the functional importance of R104 in the BH (Fig. 3c). Downstream of the target region (dG1–dC20), the ω RNA-complementary DNA strand (that is, the target strand) flipped and base-paired with the non-target DNA strand to form a TAM-containing duplex (dA[-1]-dA[-10]-dT1*-dT10*) (Fig. 1c,e). The backbone phosphate group between dC20 and dA(-1) in the target strand is recognized by Asn265 in the phosphate-lock loop, thereby facilitating heteroduplex formation (Fig. 3e). Mutating N265 to alanine reduced the nicking activity, suggesting the importance of this residue for DNA unwinding (Fig. 3c). The PLMP domain and the $\beta 7$ motif in the TI domain are the pivotal units in the RuvC-TI-PLMP scaffold (Extended Data Fig. 3a). Truncating these domains/motifs abolished the DNA nicking activity of IsrB, indicating the importance of the rigid scaffold of RuvC-TI-PLMP (Fig. 3c and Extended Data Fig. 5b). These findings show that both IsrB and the ω RNA scaffold substantially contribute to the recognition of the guide-target heteroduplex for DNA targeting.

We previously found that DtlSrB shows a NTGA TAM preference⁴, but given that DtlSrB is a thermophilic enzyme, we repeated the TAM identification assay at 60 °C. At this temperature, we observed a TTGA TAM preference (Fig. 4b). We then sought to characterize this preference structurally. The TAM-containing duplex is bound in the cleft between the WED and TI domains, in which the TAM-nucleobases in

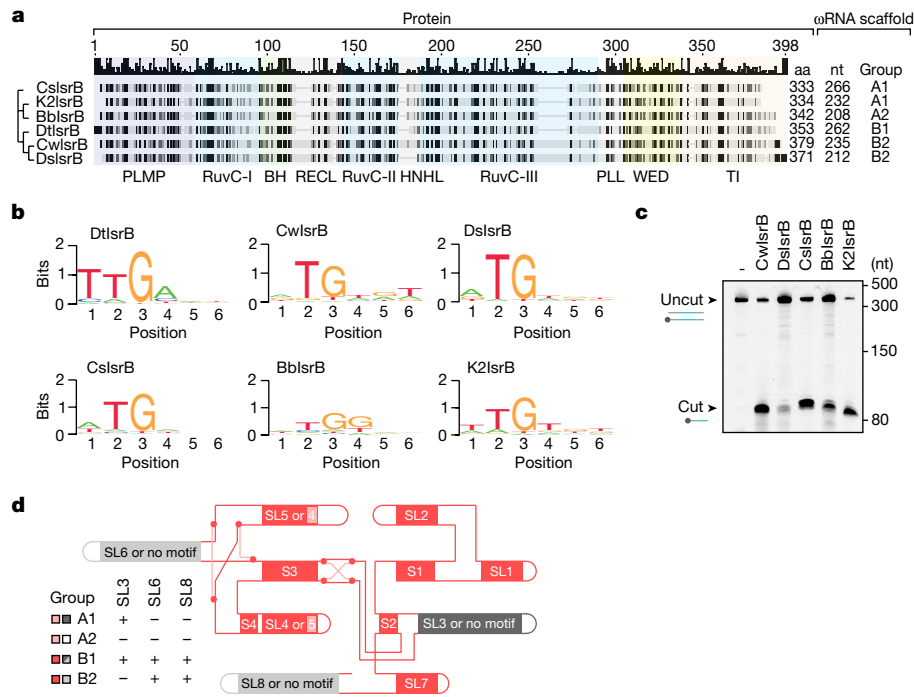


Fig. 4 | IsrB diversity. **a**, Phylogenetic tree of selected IsrB orthologues. Protein sizes are indicated, with domains highlighted in coloured boxes and conserved sequences in black. Cognate RNA sizes and groups (Fig. 4d) are indicated. **b**, TAM sequences for six IsrB orthologues using in vitro cleavage of a plasmid library containing randomized TAMs and the target sequence. **c**, In vitro reconstituted IsrB- ω RNA RNP nicking of dsDNA substrates with five IsrB orthologues. For CwlsrB, CslsrB and K2lsrB, the target DNA contained a TTGA TAM. For DlsrB and BblsrB, the target DNA contained an ATGG TAM. $n = 3$ independent technical replicates. **d**, Structural models of the ω RNA scaffolds for six IsrB orthologues based on secondary structure predictions. The predicted ω RNA scaffolds are classified into groups A (subgroup A1, CslsrB and K2lsrB; subgroup A2, BblsrB) and B (subgroup B1, DtsrB; subgroup B2,

CwlsrB and DlsrB). In group A, SL2 and SL4 form pseudoknots, and SL5 and the intermediate region between S2 and SL7 form pseudoknots. Connecting regions that differ from group B are coloured pink. The intermediate region between SL5 and S3 as well as the terminal region after SL7 ('no motif', grey) are predicted to be unpaired nucleotides. In group B, SL2 and SL5 form pseudoknots, and SL4 and the intermediate region between S2 and SL7 form pseudoknots. Connecting regions (red) are as in group A. The intermediate region between SL5 and S3 as well as the terminal region after SL7 are predicted to be stem loops (SL6 and SL8, grey). In subgroups A1 and B1, the intermediate region between S2 and S3 is predicted to be a stem loop (SL3, dark grey), whereas in subgroups A2 and B2, that region is predicted to be unpaired nucleotides ('no motif', dark grey).

the non-target strand are read out by the residues in the TI domain (Figs. 1e and 3g). Although the dT1* nucleobase does not directly contact the protein, the C5 of the dT2* nucleobase forms van der Waals interactions with that of dT1* and the aliphatic portion of the Arg323 side chain, consistent with the preference for the first and second Ts in the TAM. The O6 and N7 of dG3* interact with R323, in line with the preference for the third G of the TAM. The R323A mutant lacked cleavage activity, supporting a role for R323 in TAM recognition (Fig. 3c). The N6 and N7 of dA4* interact with Gln326, consistent with the preference for the fourth A in the TAM. To test whether Q326 recognizes the fourth TAM nucleotide, we mutated this residue to alanine and found that this mutation abolished target cleavage (Fig. 3c). The wild-type IsrB showed cleavage activity on targets with TTGA/ATGA TAMs, but not with TTGG/ATGG TAMs (Fig. 3h). However, the Q326R mutant was active with all four of these TAMs. These results indicate that Q326 recognizes the fourth nucleotide in the TAM. In SpCas9, the PAM preference can be modified through alteration of the hydrogen-bonding interactions between the amino acid at position 1,335 (Arg in wild-type SpCas9 or Gln in SpCas9 VQR-variant) and the third nucleotide of the PAM (G or A, respectively)^{13,14}. Analogously, in IsrB, the TAM preference can be modified through alteration of the hydrogen-bonding interactions between the amino acid at position 326 and the fourth nucleotide of the TAM. Together, these results indicate that DtsrB recognizes the TTGA TAM in the non-target strand by a combination of hydrogen bonds and van der Waals interactions, and indicate that altering these interactions could expand the TAM preference.

To investigate the DNA nicking mechanism of IsrB, we identified the nicked site in the DNA by Sanger sequencing. IsrB nicked the non-target strand 8–11 nt upstream of the TAM (Extended Data Fig. 6a), in contrast to Cas9s, which cleave the non-target strand 2–5 nt upstream of the PAM¹⁵. To mimic the nicked product, we added 10 nt to the 5' end of the non-target strand in the SL1-truncated IsrB complex structure (Extended Data Fig. 6b). We observed EM density of the extended part of the non-target strand, which is docked into the RuvC domain (Extended Data Fig. 6e). In the IsrB structures, the TAM and TAM-proximal parts of the non-target strand are removed from the RuvC domain (Extended Data Fig. 6e,f), whereas in the SpCas9 structure, the PAM-proximal part of the non-target strand interacts with the RuvC and HNH domains¹⁶ (Extended Data Fig. 6g). The conformational difference between the non-target strands loaded onto the RuvC domains explains the distinct location of the DNA cut made by IsrB compared to that made by SpCas9.

IsrB diversity

To assess the conservation of the ω RNA ternary structure across IsrBs, we identified five orthologues (CwlsrB, IsrB from *Crocospaera watsonii*; DlsrB, IsrB from *Dolichospermum* sp.; CslsrB, IsrB from *Calditerricola satsumensis*; BblsrB, IsrB from *Burkholderiales* bacterium; K2lsrB, IsrB discovered from contig k249_576930 of viral metagenome assembly) and their cognate ω RNAs (Fig. 4a). A TAM discovery assay showed that CwlsrB/K2lsrB/CslsrB/DlsrB recognize an NTG TAM, whereas BblsrB recognizes an NTGG TAM (Fig. 4b). We confirmed the functionality of these ω RNAs and validated the TAM preferences using

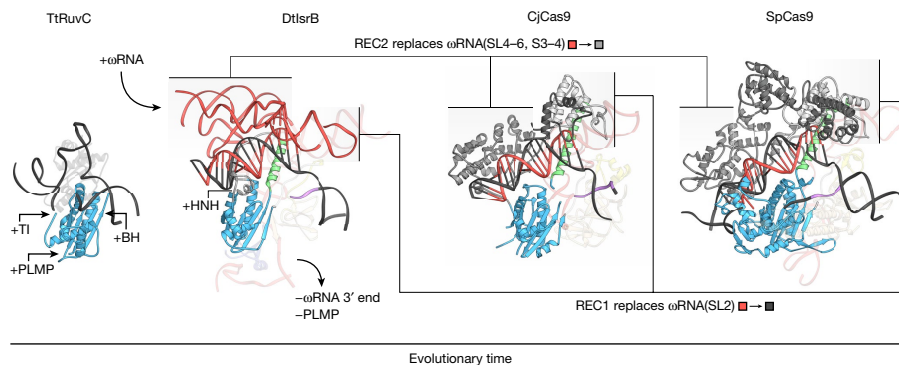


Fig. 5 | Model of IsrB evolution. Structural determinants of the evolution from ancestral RuvC nucleases to IsrB and then Cas9. Examples from modern descendants (extants) of each family are shown beginning with *T. thermophilus* RuvC (TtRuvC, PDB 6S16), DtlrB, CjCas9 (PDB 5X2G) and SpCas9 (PDB 7S4X). Critical stages in the proposed evolutionary process are shown, including the insertions of the TI, PLMP and BH domains, interaction with ω RNA, insertion of

the HNH domain, loss of the PLMP domain and replacement of various parts of the ω RNA with REC regions (domain replacements are shown with a colour key). The portion of REC2 in CjCas9 and SpCas9 that replace SL2 in the DtlrB ω RNA are coloured in a dark grey. Connected base pairing is shown only for the guide–DNA duplex. Disconnected base pairing is shown for the ω RNA adaptor pseudoknot to highlight its position near the RNA–DNA duplex.

a DNA cleavage assay with the target DNA containing the single TAM (Fig. 4c). We generated 3D structure models of these IsrB orthologues and the covariance folded two-dimensional (2D) structure models of their cognate ω RNAs (Extended Data Fig. 7). The protein 3D-model and the RNA 2D model were compatible with the experimentally determined structures of DtlrB and its cognate ω RNA, demonstrating the general reliability of structural prediction (Fig. 2a and Extended Data Fig. 7a,b). In the secondary structure prediction, the ω RNAs of DtlrB and the other five orthologues maintain the core domain composition consisting of four stems (S1–4) and five stem loops (SL1/2/4/5/7) (Fig. 4d and Extended Data Fig. 7a). In the cryo-EM structure of the DtlrB ω RNA (DtRNA), SL3, SL6 and SL8 are located at the periphery of the scaffold and do not contribute to the formation of the core (Fig. 2b). Truncation of SL8 did not appreciably affect DtlrB cleavage activity, indicating that the ω RNAs lacking this motif support at least the minimal functionality of IsrB (Fig. 2d). In the ω RNAs of CwlsrB and DslsrB, SL2 and SL5 as well as SL4 and the SL7-adjacent single-stranded region are predicted to form two pseudoknot structures, consistent with the structure of the DtRNA (Fig. 4d and Extended Data Fig. 7a). By contrast, in the ω RNAs of CslsrB, K2lsrB and BblsrB, two pseudoknot structures are predicted to be formed by SL2 and SL4 as well as SL5 and the SL7-adjacent single-stranded region (Fig. 4d and Extended Data Fig. 7a). This SL4–SL5 shuffling involved in the pseudoknot formation has been reported previously⁴ and highlights the structural robustness of ω RNAs, which maintain overall similar structures despite structural rearrangements. Taken together, the demonstrated functionality of IsrB orthologues and the predicted structural similarities of IsrBs and their ω RNAs indicate the generality of the ω RNA-guided DNA-targeting mechanism suggested by the present cryo-EM structure.

Discussion

To trace the protein domain evolution from IsrB to Cas9, we compared the structure of IsrB with the structure of one of the largest known IscBs (OgeulscB)¹⁷, a distant relative of IsrB containing the HNH nuclease domain, and the predicted structure of YnpsCas9-1 (an early branching Cas9 of subtype II-D from GaO315277_10040887 that is among the Cas9s most closely similar to IscB)⁴ (Extended Data Fig. 8). Apart from the gain of the HNH domain in IscB, we also observe big differences in other regions. For example, the RECL in some, but not all clades of IscB, is larger than the corresponding linker region in IsrB and folds into a minimal secondary structure, whereas in YnpsCas9-1, a large globular domain was acquired in the REC region. In other Cas9, such as SpCas9, this domain is even larger and more complex. The RuvC

domain in OgeulscB contains a few larger loops, whereas in YnpsCas9-1, it contains long insertions that seem to have further evolved into highly structured domains in other Cas9s including SpCas9. This enlargement of the RuvC domain in Cas9 is accompanied by the loss of the PLMP domain. Similarly, the WED and TI domains have minimal size in other IsrBs and IscBs except specifically in OgeulscB and other large IscBs in which these domains are expanded. The WED and TI domains probably continued expanding into the large, globular versions found in YnpsCas9-1 and SpCas9. SpCas9 harbours a larger PAM-interacting domain that contains an extra globular region located downstream of the common core PAM-interacting domain. The size reduction and split of the ω RNA into dual RNA guides in Cas9 (for example, tracrRNA–crRNA) probably accompanied the acquisition of the REC domain and the overall enlargement of all domains of Cas9.

To characterize in greater detail the minimization of the ω RNA as it evolved into cr/tracrRNAs, we compared the structure of DtlrB ω RNA (DtRNA) with those of OgeulscB ω RNA (OgrRNA), CjCas9 single-guide RNA (CjRNA) and SpCas9 sgRNA in their protein/target DNA-bound states (Extended Data Fig. 9)^{16–18}. On the basis of topology, location and secondary structure, we mapped DtRNA structural features (S1–4 and SL1–8) on other RNA species and named unidentified structural motifs as motifs 1–5 (M1–5). The structures of the 5'-stem region (S1 and SL1 in DtRNA) and the nexus region (S2 in DtRNA) are conserved in all four RNA species. The ascending strand of the 5'-stem region is replaced with crRNA in the evolutionary transition from OMEGA-IsrB/IscB to CRISPR–Cas9. Moreover, as ω RNAs evolved into tracrRNAs, the inserted helices (S3/S4/SL4/SL5/SL6 in DtRNA) within the nexus region degenerated, contributing to the compaction and simplification of the RNA structure. The SL4 motifs of DtRNA and OgrRNA form nexus pseudoknots that are conserved in ω RNAs, whereas some base pairings in CjRNA M3 are well superposed with those nexus pseudoknots. An embedded stem loop in DtRNA 5'-stem region (SL2) base pairs with one of the embedded stem loops in the nexus region (SL5), forming a functional pseudoknot (adaptor pseudoknot) that recognizes the target DNA. One base adjacent to the adaptor pseudoknot (C198), forms several contacts between 3 and 5 Å with the phosphate and deoxyribose moieties of the DNA at position 6 (G6) and 7 (T7) (Fig. 3a), conferring a unique adaptation in which the ω RNA scaffold can recognize the RNA–DNA duplex. The adaptor pseudoknot is conserved in IsrB ω RNAs but is degenerated in the transition to IscB ω RNAs and Cas9 tracrRNAs, a change that correlates with and is probably compensated by the REC-region expansion.

We also sought to better understand the mechanistic changes associated with the domain acquisitions in IsrB and Cas9 during their

evolution from the compact RuvC-like ancestor. To this end, we compared the target-bound structures of *Thermus thermophilus* RuvC (TtRuvC), IsrB, CjCas9 and SpCas9 (Fig. 5). As RuvC domain-containing proteins evolved to interact with ω RNAs, they acquired TI/PI, PLMP and BH domains. In the structures of both IsrB and Cas9, the RuvC, WED, TI/PI and BH domains as well as the phosphate-lock loop form a functional core with similar configurations; the guide–target heteroduplex and the TAM/PAM duplex are bound to this core in a similar position and orientation. The TI/PI domain recognizes the TAM/PAM nucleobases, probably functioning as a primer for target DNA unwinding and heteroduplex formation, with the assistance of the phosphate-lock loop, BH and ω RNA/gRNA. Although IsrB and Cas9 share homologous RuvC and BH domains, IsrB (as well as IscB) uniquely contains the PLMP domain, which directly interacts with RuvC I. Examination of the IsrB structure further reveals a role of the PLMP domain in stabilizing the base of the terminal hairpin of the ω RNA and contacting the Shine–Dalgarno sequence. Furthermore, IsrB contains only minimal RECL and HNHL regions (17 and 19 amino acids, respectively, in DtlrB), and they probably play different roles in DNA targeting from those performed by the larger REC lobe and HNH domain in Cas9 (for example, 625 and 135 amino acids, respectively, in SpCas9). In SpCas9, the REC lobe probes the target DNA through interactions with the heteroduplex, activates the DNA-bound RuvC nuclease through the communication with the HNH domain and facilitates R-loop formation^{19–21}. However, in IsrB, this interdomain communication is probably aided by the ω RNA both through backbone–backbone and base–backbone interactions because RECL and HNHL are comparatively small.

The comparatively large ω RNA (roughly 300-nt compared to 100-nt sgRNA used by Cas9) seems to contribute to the connection between DNA targeting and nicking activities, compensating for the small RECL and HNHL regions (Extended Data Fig. 10). In the multi-layered ω RNA architecture, the upper layer RNA helices (S2/S3/S4/SL2/SL4/SL5), which form an interaction network for ω RNA-driven heteroduplex recognition, are associated with the lower layer RNA helices (SL7/SL8) and extensively interact with the nicking module (PLMP/RuvC/TI domains) by the nexus pseudoknot interactions between S2, SL4 and SL7. Given that mutations in the adaptor pseudoknot in the ω RNA abolished the nicking activity of IsrB (Fig. 2d), even though the pseudoknot is distant from the target DNA, the ω RNA structural motifs could be important for allosteric regulation of DNA sensing by the ω RNA/RECL and DNA nicking by the RuvC nuclease domain, providing an avenue for integrating further forms of regulation. This ω RNA-driven allosteric regulation mechanism is supported by the overall high surface charge and area through which IsrB contacts ω RNA. Other large (roughly 400–900-nt) functional non-coding RNAs, such as group I intron, group II intron and Ribonuclease P, have complex ternary structures and their peripheral regions can control their central catalytic cores by allosteric mechanisms^{22–25}. Future structural studies of IsrB in other conformations, such as the catalytically active IsrB R-loop complex, will address this hypothesis and deepen our mechanistic understanding of OMEGA systems.

Online content

Any methods, additional references, Nature Research reporting summaries, source data, extended data, supplementary information,

acknowledgements, peer review information; details of author contributions and competing interests; and statements of data and code availability are available at <https://doi.org/10.1038/s41586-022-05324-6>.

- Zhang, F. Development of CRISPR–Cas systems for genome editing and beyond. *Q. Rev. Biophys.* **52**, e6–e6 (2019).
- Doudna, J. A. The promise and challenge of therapeutic genome editing. *Nature* **578**, 229–236 (2020).
- Nishimasu, H. & Nureki, O. Structures and mechanisms of CRISPR RNA-guided effector nucleases. *Curr. Opin. Struct. Biol.* **43**, 68–78 (2017).
- Altae-Tran, H. et al. The widespread IS200/IS605 transposon family encodes diverse programmable RNA-guided endonucleases. *Science* **374**, 57–65 (2021).
- Kapitonov, V. V., Makarova, K. S. & Koonin, E. V. ISC, a novel group of bacterial and archaeal DNA transposons that encode Cas9 homologs. *J. Bacteriol.* **198**, 797–807 (2015).
- Afonine, P. V. et al. Real-space refinement in PHENIX for cryo-EM and crystallography. *Acta Crystallogr. Sect. D, Struct. Biol.* **74**, 531–544 (2018).
- Croll, T. I. ISOLDE: a physically realistic environment for model building into low-resolution electron-density maps. *Acta Crystallogr. Sect. D, Struct. Biol.* **74**, 519–530 (2018).
- Kappel, K. et al. Accelerated cryo-EM-guided determination of three-dimensional RNA-only structures. *Nat. Methods* **17**, 699–707 (2020).
- Briner, A. E. et al. Guide RNA functional modules direct Cas9 activity and orthogonality. *Mol. Cell* **56**, 333–339 (2014).
- He, S. et al. The IS200/IS605 family and ‘peel and paste’ single-strand transposition mechanism. *Microbiology Spectr.* <https://doi.org/10.1128/microbiolspec.MDNA3-0039-2014> (2015).
- Juneau, K., Podell, E., Harrington, D. J. & Cech, T. R. Structural basis of the enhanced stability of a mutant ribozyme domain and a detailed view of RNA–solvent interactions. *Structure* **9**, 221–231 (2001).
- Jiang, F., Zhou, K., Ma, L., Gressel, S. & Doudna, J. A. A Cas9–guide RNA complex preorganized for target DNA recognition. *Science* **348**, 1477–1481 (2015).
- Hirano, S., Nishimasu, H., Ishitani, R. & Nureki, O. Structural basis for the altered PAM specificities of engineered CRISPR–Cas9. *Mol. Cell* **61**, 886–894 (2016).
- Kleinstiver, B. P. et al. Engineered CRISPR–Cas9 nucleases with altered PAM specificities. *Nature* **523**, 481–485 (2015).
- Ran, F. A. et al. In vivo genome editing using *Staphylococcus aureus* Cas9. *Nature* **520**, 186–191 (2015).
- Bravo, J. P. K. et al. Structural basis for mismatch surveillance by CRISPR–Cas9. *Nature* **603**, 343–347 (2022).
- Schuler, G., Hu, C. & Ke, A. Structural basis for RNA-guided DNA cleavage by IscB- ω RNA and mechanistic comparison with Cas9. *Science* **376**, 1476–1481 (2022).
- Yamada, M. et al. Crystal structure of the minimal Cas9 from *Campylobacter jejuni* reveals the molecular diversity in the CRISPR–Cas9 systems. *Mol. Cell* **65**, 1109–1121.e3 (2017).
- Chen, J. S. et al. Enhanced proofreading governs CRISPR–Cas9 targeting accuracy. *Nature* **550**, 407–410 (2017).
- Sternberg, S. H., LaFrance, B., Kaplan, M. & Doudna, J. A. Conformational control of DNA target cleavage by CRISPR–Cas9. *Nature* **527**, 110–113 (2015).
- Pacesa, M. et al. R-loop formation and conformational activation mechanisms of Cas9. *Nature* **609**, 191–196 (2022).
- Haack, D. B. et al. Cryo-EM structures of a group II intron reverse splicing into DNA. *Cell* **178**, 612–623.e12 (2019).
- Reiter, N. J. et al. Structure of a bacterial ribonuclease P holoenzyme in complex with tRNA. *Nature* **468**, 784–789 (2010).
- Su, Z. et al. Cryo-EM structures of full-length Tetrahymena ribozyme at 3.1 Å resolution. *Nature* **596**, 603–607 (2021).
- Weinberg, Z., Perreault, J., Meyer, M. M. & Breaker, R. R. Exceptional structured noncoding RNAs revealed by bacterial metagenome analysis. *Nature* **462**, 656–659 (2009).

Publisher's note Springer Nature remains neutral with regard to jurisdictional claims in published maps and institutional affiliations.



Open Access This article is licensed under a Creative Commons Attribution 4.0 International License, which permits use, sharing, adaptation, distribution and reproduction in any medium or format, as long as you give appropriate credit to the original author(s) and the source, provide a link to the Creative Commons license, and indicate if changes were made. The images or other third party material in this article are included in the article's Creative Commons license, unless indicated otherwise in a credit line to the material. If material is not included in the article's Creative Commons license and your intended use is not permitted by statutory regulation or exceeds the permitted use, you will need to obtain permission directly from the copyright holder. To view a copy of this license, visit <http://creativecommons.org/licenses/by/4.0/>.

© The Author(s) 2022

Methods

Electron microscopy sample preparation

The gene encoding full-length DtlrB (residues 1–353) was codon optimized, synthesized (Twist Bioscience) and cloned into a modified pC013 vector (Addgene Plasmid no. 90097). The DtlrB-coding region consists of His₆-Twinstrep-tag, SUMO-tag, DtlrB and GFP-tag. Wild-type DtlrB was expressed at 18 °C in *Escherichia coli* Rosetta (DE3) pLysS cells (Novagen). *E. coli* was cultured at 37 °C in Luria-Bertani medium (containing 100 mg l⁻¹ ampicillin) until the OD₆₀₀ reached 0.5, and then protein expression was induced by the addition of 0.1 mM isopropyl-β-D-thiogalactopyranoside and incubation at 18 °C for 20 h. The *E. coli* cells were resuspended in buffer A (50 mM Tris-HCl, pH 8.0, 20 mM imidazole and 1 M NaCl), lysed by sonication and then centrifuged. The supernatant was mixed with Ni-NTA Agarose (Qiagen). The protein-bound column was washed with buffer A, buffer B (50 mM Tris-HCl, pH 8.0, 20 mM imidazole and 0.3 M NaCl) and buffer C (50 mM Tris-HCl, pH 8.0, 0.3 M imidazole and 0.3 M NaCl). The protein was eluted with buffer D (50 mM Tris-HCl, pH 8.0, 0.3 M imidazole and 1 M NaCl). The cognate ωRNA of DtlrB was transcribed in vitro with T7 RNA polymerase, using a PCR-amplified DNA template and HiScribe T7 Quick High Yield RNA Synthesis kit (NEB). The template consists of the T7 promoter (TAATACGACTCACTATAGG), guide (GCCTTATTAATGACTTCTC) (residues 1–20) and ωRNA scaffold (residues 21–282). The transcribed RNA was purified using an RNeasy kit (Qiagen) according to the manufacturer's instructions. The target and non-target DNA strands (GATCAGCTCAAGAGAAGTCATTAATAAGGC and TTGAGCTGAT, respectively) were purchased from GENEWIZ. For the reconstitution of complex A, the purified DtlrB protein was mixed with the ωRNA, the target DNA strand and the non-target DNA strand (the TTGA TAM) (molar ratio, 2.3:1:7:7) in buffer E (10 mM Tris-HCl, pH 8.0 and 50 mM NaCl, 5 mM MgCl₂) and incubated at 37 °C for 15 min. Complex A was purified by gel filtration chromatography on a Superose 6 Increase 10/300 column (Cytiva) equilibrated with buffer F (20 mM HEPES-NaOH, pH 7.0 and 50 mM NaCl, 5 mM MgCl₂). Complex A (final concentration: 0.1 mg ml⁻¹) was incubated with BS3 (final concentration: 0.5 mM) at 4 °C for 2 h. For the reconstitution of complex B, the lambda N protein (MDAQRTRRRERRAEKQAQWKAAN) was inserted between DtlrB and GFP-tag. Residues 34–67 of ωRNA scaffold (residues 21–282) were replaced by a GAAA linker. The GAAA linker-fused boxB RNA (GAAAGCCUGAAGAAGGGC) (residues 283–302) was appended to the 3' end of the ωRNA scaffold. The same target DNA strand was used for this reconstitution. The 5' extended non-target DNA strand (TACTGAAGAGTTGAGCTGAT) was purchased from GENEWIZ. The purified DtlrB protein was mixed with the ωRNA, the target DNA strand, and the non-target DNA strand (the TTGA TAM) (molar ratio, 2.3:1:1.5:1.5) in buffer G (10 mM Tris-HCl, pH 8.0 and 50 mM NaCl) and incubated at 37 °C for 15 min. Complex B was purified by the same size-exclusion column equilibrated with buffer G. For the grid preparation, purified complex A and B solutions (0.1 mg ml⁻¹, 3 μl) were applied to freshly glow-discharged UltrAuFoil 300 mesh R1.2/1.3 grids (Quantifoil) in a Vitrobot Mark IV (FEI) at 4 °C with a waiting time of 0 and 10 s and a blotting time of 2 and 4 s under 95% humidity, respectively.

Electron microscopy data collection and processing

Cryo-EM data for complex A were collected at HHMI Janelia Research Campus using a Titan Krios G2 microscope (Thermo), operated at 300 kV and equipped with a Gatan Bioquantum energy filter (Gatan) and a postfilter K3 direct electron detector (Gatan) in the electron counting mode. Each video was recorded at a nominal magnification of ×105,000, corresponding to a 0.839 Å per physical pixel (0.4195 Å per super-resolution pixel) at the electron exposure of 12.075 electrons per Å² per second and total exposure time was 5.0 s, resulting in an accumulated exposure of 60 e⁻/Å². Then 50 frames per video were collected at

1.2 e⁻/Å² dose per frame for a total of 60 e⁻/Å² dose per video. The nominal defocus range was set at -0.8 to -2.2 μm. Automated data collection was carried out using scripts in SerialEM. For each stage position, image shift was used to collect data from nine holes with two video acquisitions per hole. Image shift induced beam tilt was calibrated and beam-tilt correction was applied during the data collection. Cryo-EM data for complex B were collected at MIT.nano using a Talos Arctica G2 microscope (FEI), operated at 200 kV and equipped with a Falcon 3EC direct electron detector (Thermo) in the linear mode. Each video was recorded at a nominal magnification of ×120,000, corresponding to a calibrated pixel size of 1.2550 Å at the electron exposure of 24.54 e⁻/pix s⁻¹ for 3.99 s, resulting in an accumulated exposure of 62.53 e⁻/Å². Next, 20 frames per video were collected at 3.1265 e⁻/Å² dose per frame for a total of 62.53 e⁻/Å² dose per video. The nominal defocus range was set at -2.6 to -1.0 μm. Automated data collection was carried out using the EPU software (Thermo). For each stage position, image shift was used to collect data from nine holes. To obtain the 3D reconstruction of complex A, data were processed using RELION-4.0 (ref. 26). The video frames were aligned in 5 × 5 patches and dose weighted in Motion-Cor2 (ref. 27). Defocus parameters were estimated by CTFFIND-4.1 (ref. 28). From the 4,142 preprocessed micrographs, 1,626,574 particles were picked up by TOPAZ based auto-picking²⁹ and extracted in 3.146 Å pixel⁻¹. The selected 107,066 particles were then re-extracted in 1.144 Å pixel⁻¹ and subjected to one round of 3D refinement and 3D classification without alignment. The selected 58,188 particles were subjected to per-particle defocus estimation and Bayesian polishing. For beam-tilt refinement, the optics group of each micrograph is set on the basis of their hole position from stage. The polished particles were subjected to 3D refinement, and yielded a map with a global resolution of 3.10 Å according to the Fourier shell correlation 0.143 criterion. To obtain the 3D reconstruction of complex B, data were processed using the same programs. From the 2,542 motion-corrected and dose-weighted micrographs, 1,595,800 particles were picked up by TOPAZ based auto-picking and extracted in 3.138 Å pixel⁻¹. These particles were subjected to several rounds of 2D and 3D classifications. The selected 50,661 particles were then re-extracted in 1.255 Å pixel⁻¹ and subjected to homogeneous refinement using cryoSPARC³⁰, yielding a map with a global resolution of 6.85 Å according to the Fourier shell correlation 0.143 criterion.

Model building and validation

The initial protein model was generated using AlphaFold2 (ref. 31) under the ColabFold framework using default parameters and MMseqs2 to search for homologues into the ColabFold database³², and manually modified using COOT³³ and ISOLDE⁷ against the density map of complex A. The initial nucleic acid model was built with auto-DRRAFTER using the density map of complex A and the covariance-based secondary structure model of ωRNA⁸. The ωRNA (query) secondary structures were predicted using cmsearch³⁴ with the -max option to identify the highest scoring IscB/IsrB ωRNA covariance model from a previous study⁴. For the best model, query regions aligning to the model were assigned secondary structures from the model's predictions. Stem loop secondary structures that were found to be erroneously assigned to base pairs with one of the base identities equalling a gap character were reassigned to having no secondary structure. Secondary structures for query regions without coverage (≥8 bp of no match to the best covariance model), barring the low conservation region at the 3' end beyond the nexus, were then predicted using mfold³⁵. Pseudoknots were assigned manually by identifying matching base pairs at the pseudoknot locations expected for the given ωRNA type. ωRNA coordinates were modelled with auto-DRRAFTER starting from a slightly modified version of the covariance-based secondary structure model in which all non-canonical base pairs and most helices consisting of just a single base pair were removed. The dot-bracket notation for this secondary structure is provided below:

Article

cloned into pUC19 by Gibson cloning (NEB) to generate a TAM library. The library (25 ng) was digested using an in vitro transcription/translation expression system containing the IrsB protein (50 ng) and ω RNA (125 ng) templates, as described in the in vitro cleavage experiment section. The reactions of CwIrsB, DsIrsB, CslsB, BbIrsB and K2IrsB were incubated for 4 h: 2 h at 37 °C, 1 h at 50 °C and 1 h at 60 °C. The reaction of DtlrsB was incubated for 3 h: 2 h at 37 °C and 1 h at 60 °C. It was then stopped by the addition of 3 μ g of RNase A (Qiagen) and 0.24 units of Proteinase K (NEB). The reaction products were purified using a Wizard SV Gel and PCR Clean-Up System (Promega), and digested using Nb.BbvCI (NEB). The purified reaction products were subjected to end labelling and adaptor ligation using an NEBNext Ultra II End Repair/dA-Tailing Module (NEB), an NEBNext Ultra II DNA Library Prep Kit for Illumina (NEB) and an NEBNext Adaptor for Illumina (NEB). The USER Enzyme (NEB)-digested and purified DNA was amplified with a 12-cycle PCR using one primer specific to the TAM library backbone and one primer specific to the NEBNext adaptor, and with a subsequent 18-cycle PCR to add the Illumina i5 adaptor. To normalize the distribution of the 8N degenerate flanking sequences, the library plasmid was amplified with a 12-cycle PCR using primers specific to the library backbone and with a subsequent 18-cycle PCR to add the Illumina i5 adaptor. The amplified libraries were isolated on 2% agarose E-gels (Invitrogen) and sequenced on a MiSeq sequencer (Illumina). The resulting sequence data were analysed by extracting the six nucleotide TAM regions, counting the individual TAMs and normalizing the TAM to the total reads for each sample. Sequence motifs were generated using the selected TAMs in the top scoring fraction with the custom Python script used in our previous report⁴.

Reporting summary

Further information on research design is available in the Nature Research Reporting Summary linked to this article.

Data availability

The atomic coordinates of the IrsB ternary structure have been deposited with the Protein Data Bank (PDB) at <http://www.pdb.org> (PDB 8DMB). The three-dimensional cryo-EM reconstructions of complex A and complex B have been deposited with the Electron Microscopy Data Bank (complex A EMD27533; complex B EMD26723).

- Kimanius, D., Dong, L., Sharov, G., Nakane, T. & Scheres, S. H. W. New tools for automated cryo-EM single-particle analysis in RELION-4.0. *Biochem. J* **478**, 4169–4185 (2021).
- Zheng, S. Q. et al. MotionCor2: anisotropic correction of beam-induced motion for improved cryo-electron microscopy. *Nat. Methods* **14**, 331–332 (2017).

- Rohou, A. & Grigorieff, N. CTFFIND4: fast and accurate defocus estimation from electron micrographs. *J. Struct. Biol.* **192**, 216–221 (2015).
- Bepko, T. et al. Positive-unlabeled convolutional neural networks for particle picking in cryo-electron micrographs. *Nat. Methods* **16**, 1153–1160 (2019).
- Punjani, A., Rubinstein, J. L., Fleet, D. J. & Brubaker, M. A. cryoSPARC: algorithms for rapid unsupervised cryo-EM structure determination. *Nat. Methods* **14**, 290–296 (2017).
- Jumper, J. et al. Highly accurate protein structure prediction with AlphaFold. *Nature* **596**, 583–589 (2021).
- Mirdita, M., et al. ColabFold: making protein folding accessible to all. *Nat. Methods* **19**, 679–682 (2022).
- Emsley, P., Lohkamp, B., Scott, W. G. & Cowtan, K. Features and development of Coot. *Acta Crystallogr. D., Biol. Crystallogr.* **66**, 486–501 (2010).
- Nawrocki, E. P. & Eddy, S. R. Infernal 1.1: 100-fold faster RNA homology searches. *Bioinformatics* **29**, 2933–2935 (2013).
- Zuker, M. Mfold web server for nucleic acid folding and hybridization prediction. *Nucleic Acids Res.* **31**, 3406–3415 (2003).
- Williams, C. J. et al. MolProbity: more and better reference data for improved all-atom structure validation. *Protein Sci.* **27**, 293–315 (2018).
- Pintilie, G. et al. Measurement of atom resolvability in cryo-EM maps with Q-scores. *Nat. Methods* **17**, 328–334 (2020).
- Kaksonen, A. H., Spring, S., Schumann, P., Kroppenstedt, R. M. & Puhakka, J. A. *Desulfovibrio thermocuniculi* gen. nov., sp. nov., a thermophilic sulfate-reducer isolated from a geothermal underground mine in Japan. *Int. J. Syst. Evol. Microbiol.* **57**, 98–102 (2007).
- Kerpedjiev, P., Hammer, S. & Hofacker, I. L. Forna (force-directed RNA): simple and effective online RNA secondary structure diagrams. *Bioinformatics* **31**, 3377–3379 (2015).

Acknowledgements We thank E. Brignole, C. Borsa, X. Zhao and S. Yang for assistance with cryo-EM grid preparation and data collection. Specimens were prepared and imaged at the Cryogenic-Electron Microscopy Facility in MIT.nano, established in part with financial support from the Arnold and Mabel Beckman Foundation. We thank all members of the Zhang laboratory for helpful discussions and support. S.H. is supported by a JSPS Overseas Research Fellowship. K.K. is supported by the Schmidt Science Fellows, in partnership with the Rhodes Trust, and the HHMI Hanna H. Gray Fellows Program. F.Z. is supported by National Institutes of Health (grant nos. 1DP1-HL141201 and 2R01HG009761-05); the Howard Hughes Medical Institute; the Poitras Center for Psychiatric Disorders Research at MIT; the Hock E. Tan and K. Lisa Yang Center for Autism Research at MIT; the Yang-Tan Molecular Therapeutics Center at McGovern, the BT Charitable Foundation and by the Phillips family and J. and P. Poitras.

Author contributions S.H. and F.Z. conceived the project. S.H., K.K., G.F., H.A.-T., M.E.W., S.K., F.E.D. and K.S.M. designed and performed experiments and analysed the results. R.Y., M.S. and Z.Y. performed data collection. F.Z. supervised the research and experimental design with support from R.K.M. S.H., R.K.M., E.V.K. and F.Z. wrote the manuscript with input from all authors.

Competing interests F.Z. is a scientific adviser and cofounder of Editas Medicine, Beam Therapeutics, Pairwise Plants, Arbor Biotechnologies and Proof Diagnostics.

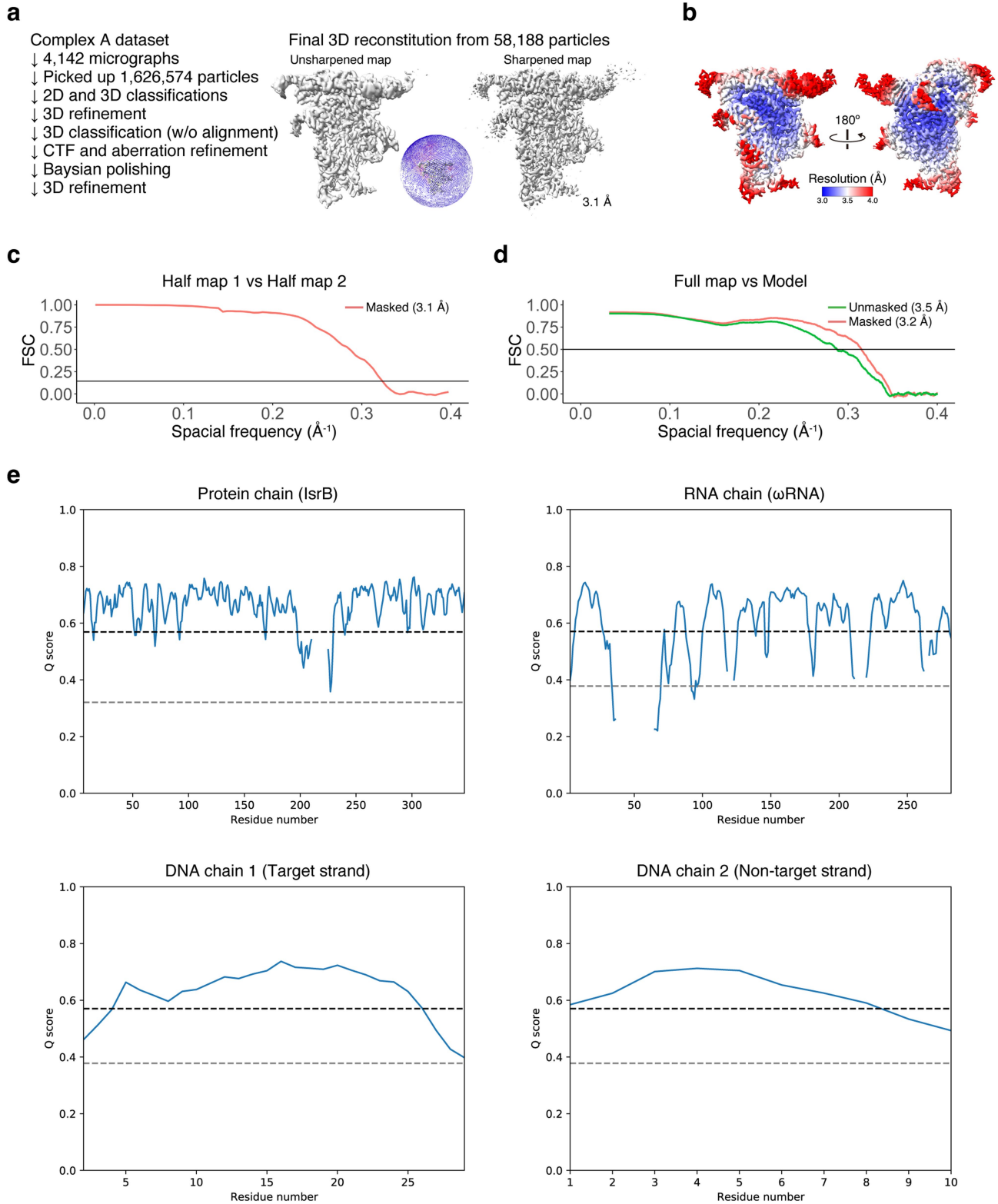
Additional information

Supplementary information The online version contains supplementary material available at <https://doi.org/10.1038/s41586-022-05324-6>.

Correspondence and requests for materials should be addressed to Feng Zhang.

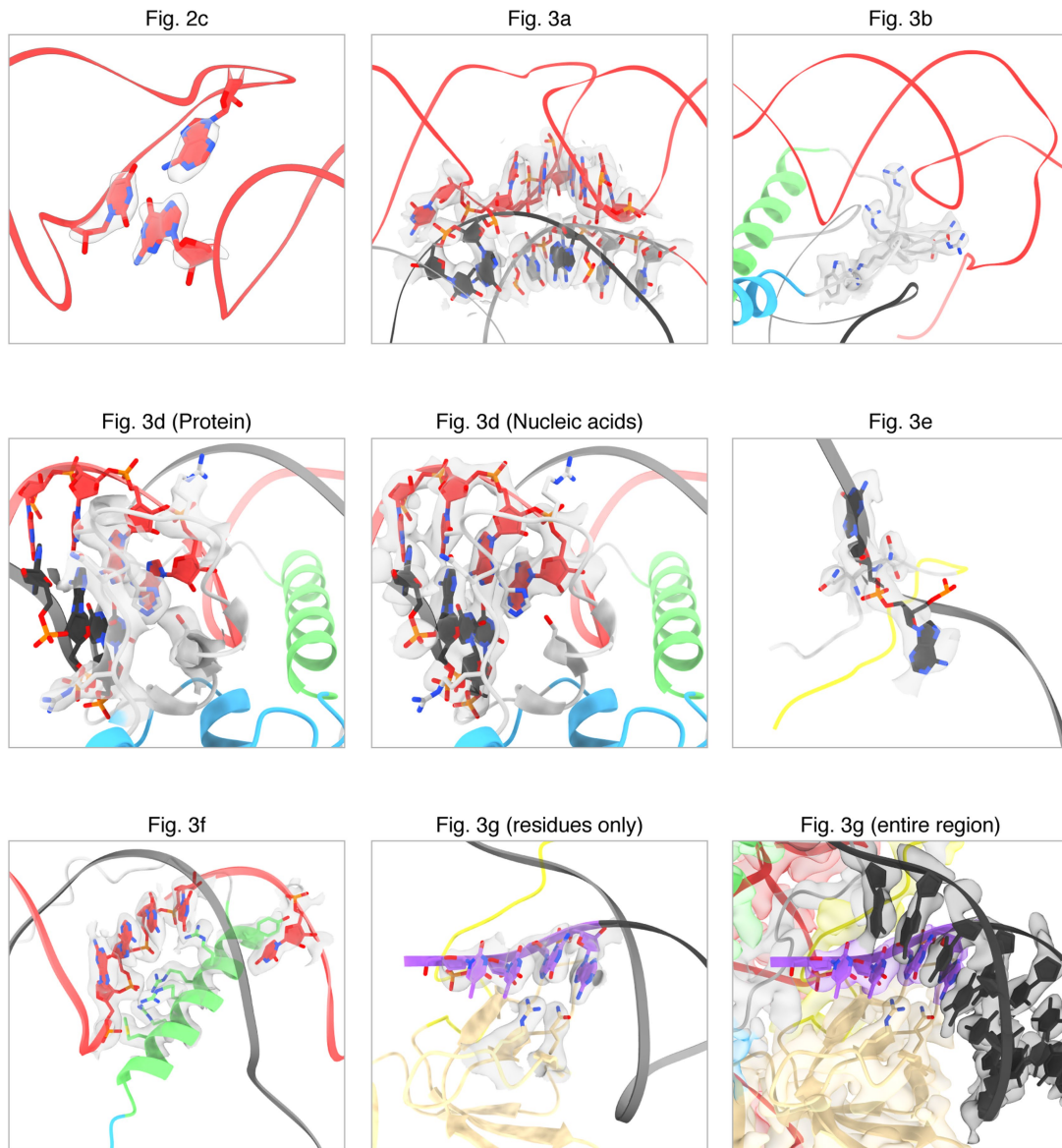
Peer review information Nature thanks Malcolm White, David Taylor and the other, anonymous, reviewer(s) for their contribution to the peer review of this work. Peer reviewer reports are available.

Reprints and permissions information is available at <http://www.nature.com/reprints>.



Extended Data Fig. 1 | Cryo-EM data processing for the IsrB- ω RNA-DNA complex (complex A). (a) Cryo-EM data processing schematic for single particle analysis of the complex A. Unsharpened (Left) and sharpened (Right) maps in the final 3D refinement. Particle orientation distribution (Center). (b) Final refined map, colored by local resolution, calculated in RELION-4.0 with FSC threshold 0.5. (c) FSC curves calculated between the half maps of complex A from the final round of the refinement in RELION-4.0. (d) FSC curves

calculated between the model and the final refined map, using phenix.validation_cryoem. (e) Q-scores for each residue of IsrB- ω RNA-target strand DNA-non-target strand DNA model in 3.1 Å map of the IsrB- ω RNA-DNA complex. The dashed black and grey lines in the plot represent the expected Q-scores based on the global map resolution (3.1 Å) and the local map resolution (4.5 Å), respectively. Q-scores for the RNA and DNA residues are consistent with the expected values based on the local map resolution.

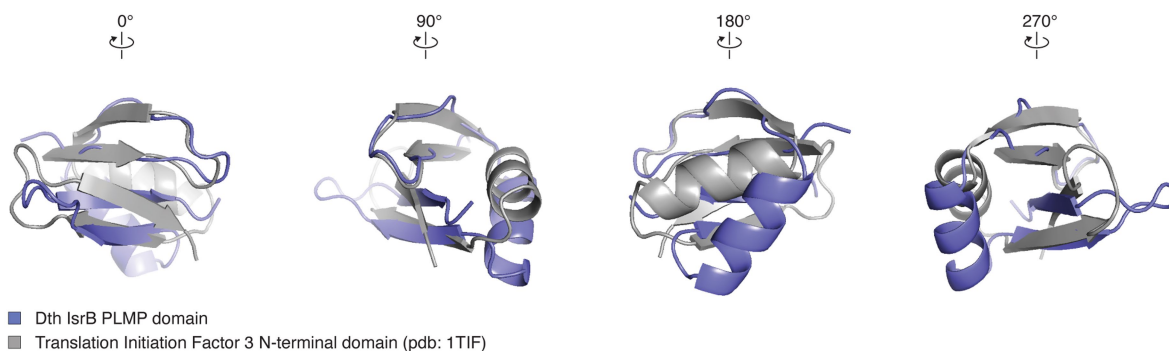


Extended Data Fig. 2 | Cryo-EM density maps. Cryo-EM density maps for residues represented in main figures.

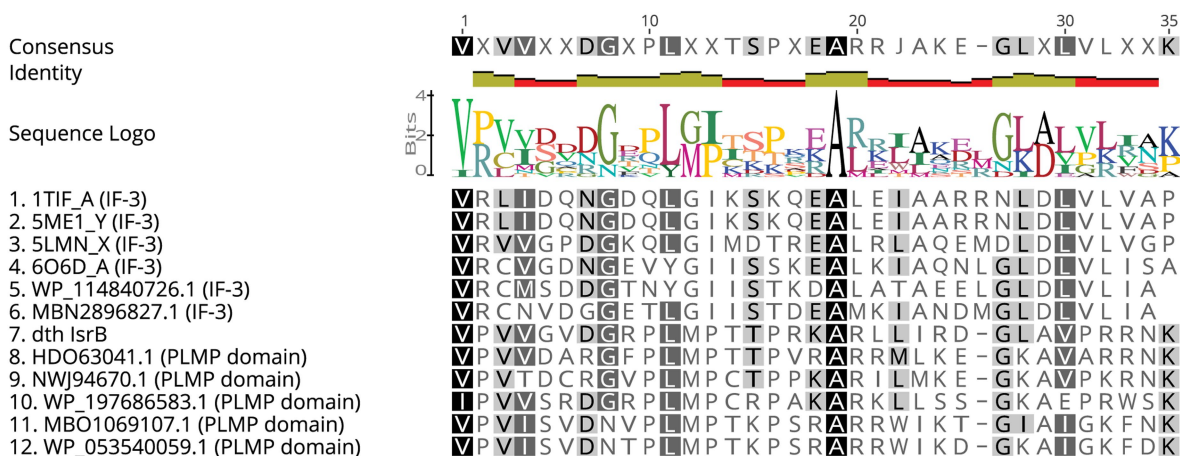
a

Nr	Hit	Name	Probability	E-value	Score	SS	Aligned cols	Target Length
<input type="checkbox"/> 1	PF14239.9	; RRXRR; RRXRR protein	99.67	2.7e-16	96.14	5.9	44	173
<input type="checkbox"/> 2	PF20090.2	; DUF6482; Family of unknown function (DUF6482)	56.42	43	18.9	2.9	26	99
<input type="checkbox"/> 3	cd14836	AP2_Mu_N; AP-2 complex subunit mu N-terminal domain. AP-2 complex mu subunit is part of the heterotetrameric adaptor pro	52.6	24	19.4	1.5	15	140
<input type="checkbox"/> 4	1TIF_A	TRANSLATION INITIATION FACTOR 3; IF3 N-TERMINAL DOMAIN, RIBOSOME BINDING FACTOR; 1.8A {Geobacillus stearothermophilus} S	52.21	70	17.52	3.5	33	78
<input type="checkbox"/> 5	PF18225.4	; AbfS_sensor; Sensor histidine kinase (AbfS) sensor domain	50.71	27	19.37	1.4	12	65

b



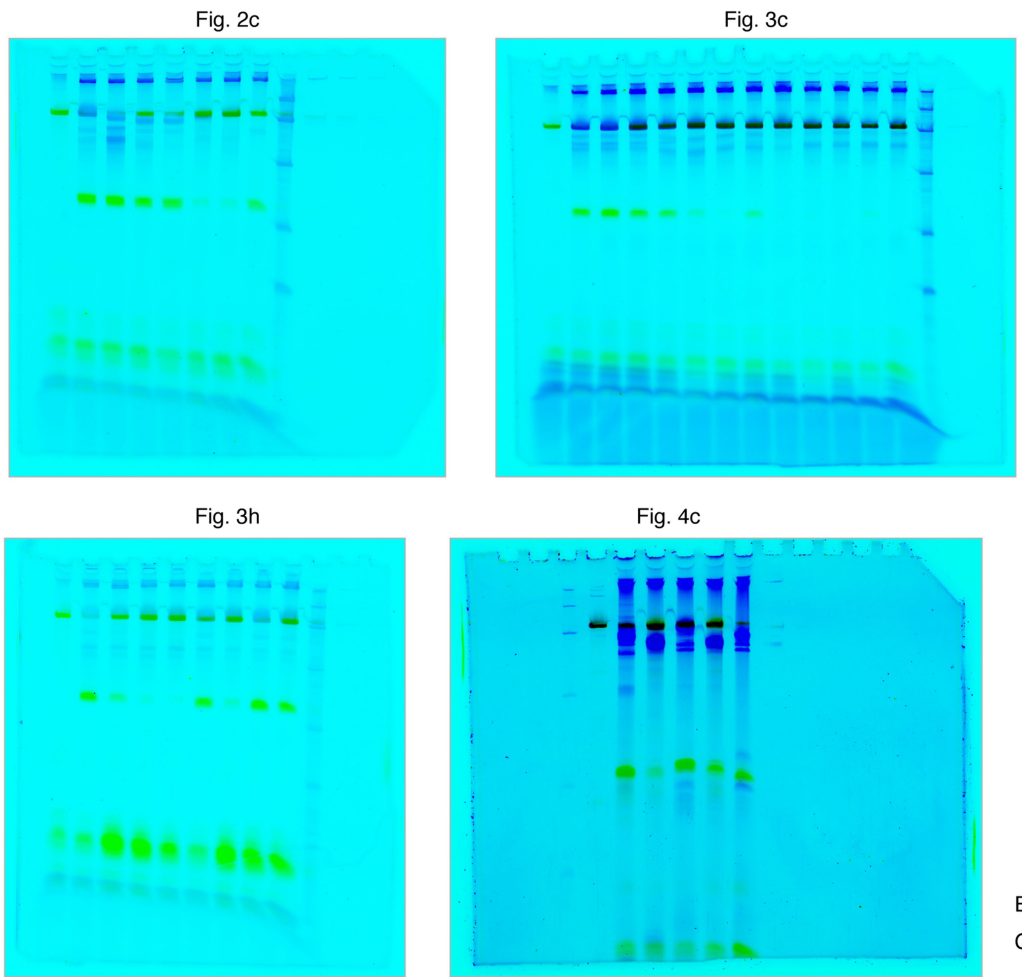
c



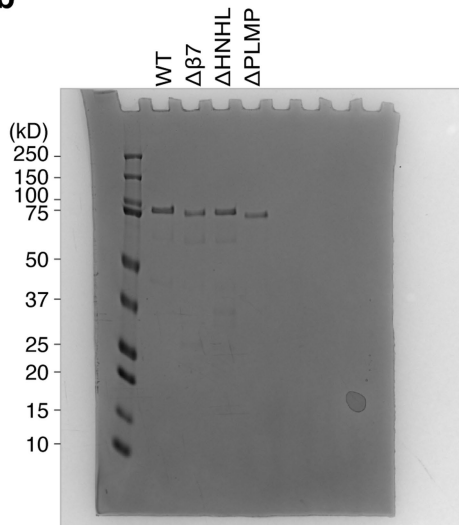
Extended Data Fig. 4 | PLMP domain homology. (a) Top five hits from HHPred search using seed sequence SITRVVVGVDGRPLMPTTPRKARLLIRDGLAVPR RNKLGIFYIQMLRPVGTTRTQ corresponding to the PLMP domain from DtlSrB. (b) Structural comparison of the PLMP domain from DtlSrB and the N-terminal

domain of Translation Initiation Factor 3 (IF-3) from *Geobacillus stearothermophilus* (PDB: 1TIF). (c) Alignment of representative IF-3 N-terminal domains and OMEGA-related PLMP domains.

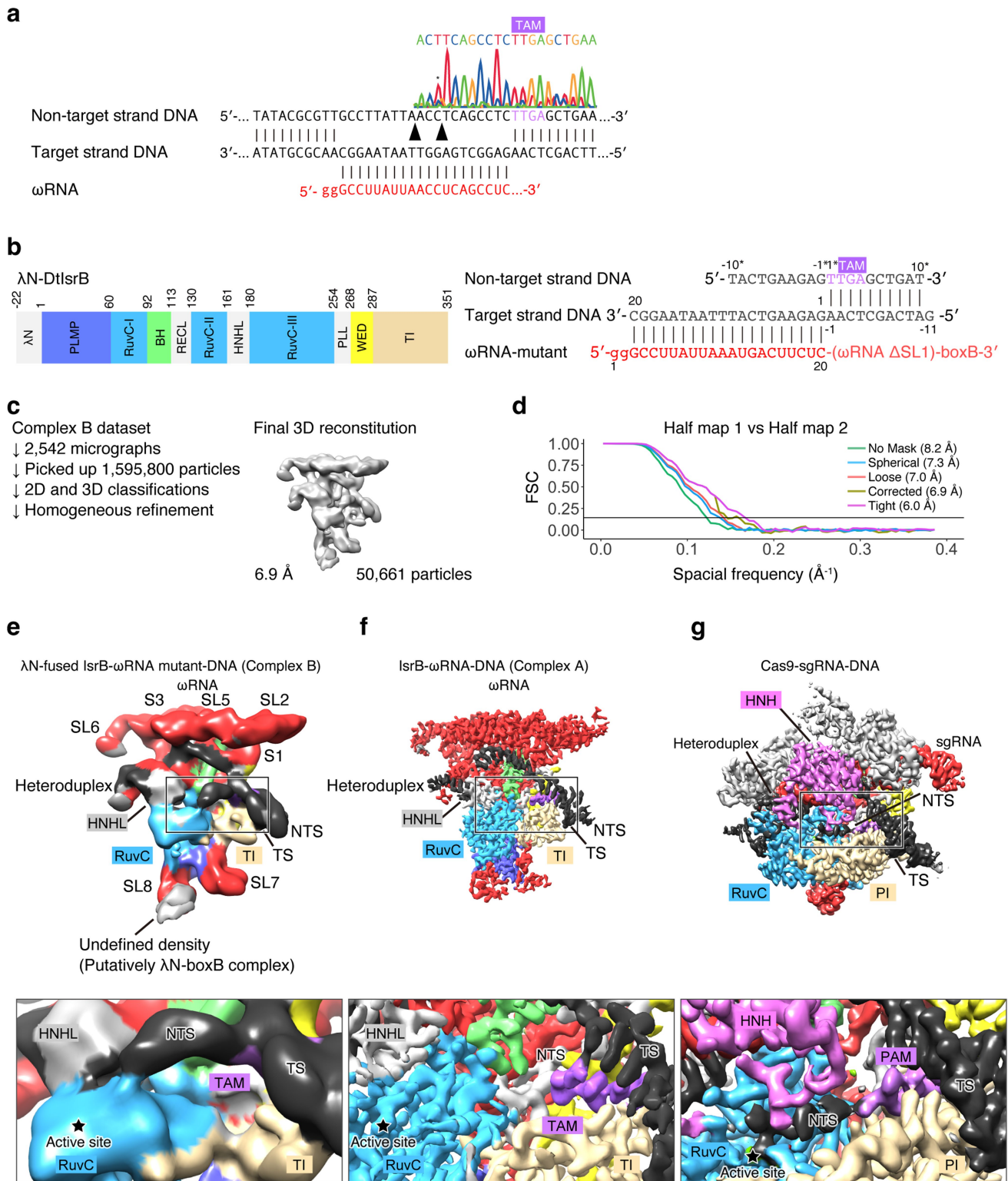
a



b



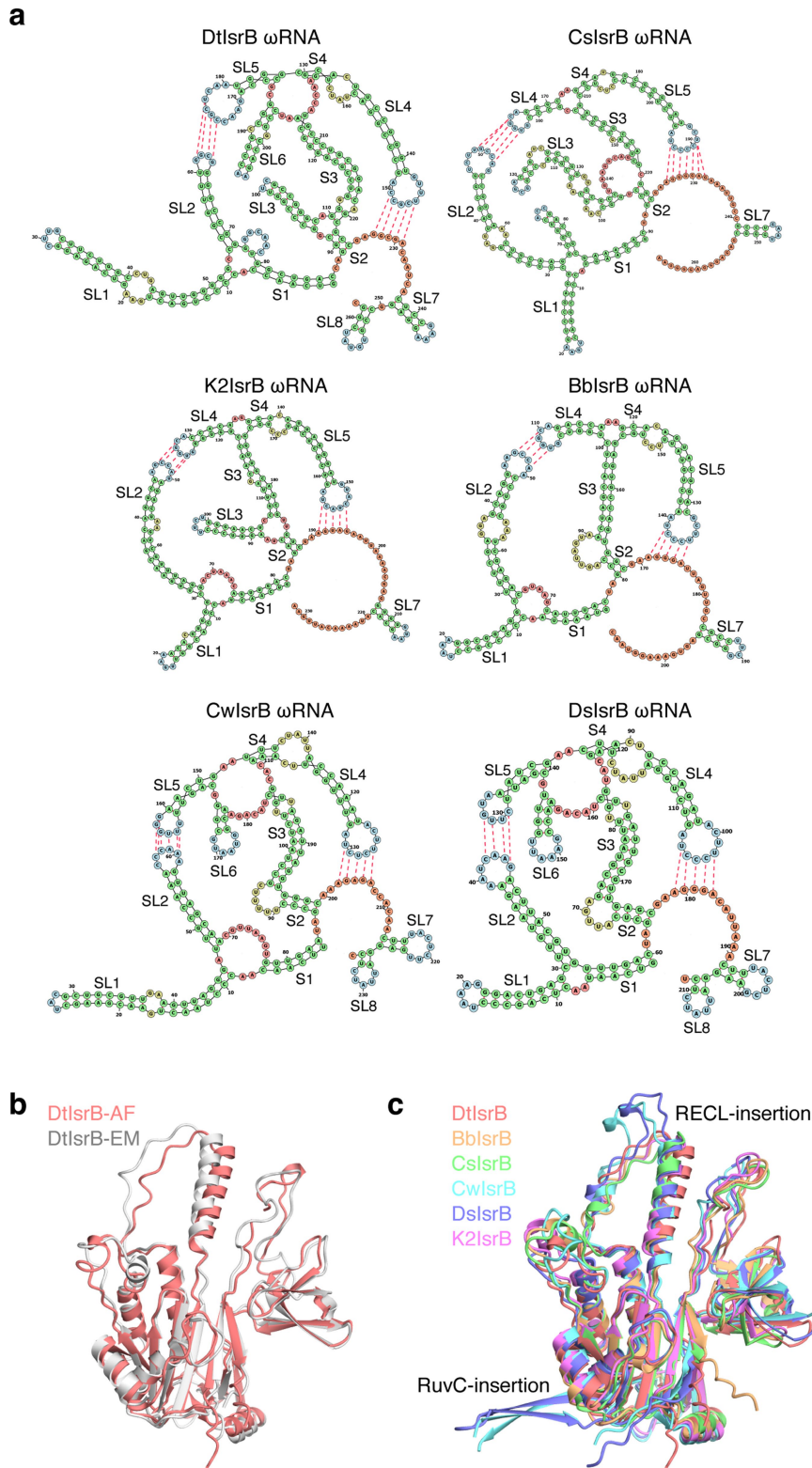
Extended Data Fig. 5 | Uncropped gel images used in this study. (a) Denatured PAGE gels for resolving nicked DNA products. (b) An SDS-PAGE gel for expression check of the deletion mutants. Related to Fig. 3c.



Extended Data Fig. 6 | Cryo-EM structure of the λ N-IsrB- ω RNA mutant-DNA complex (complex B).

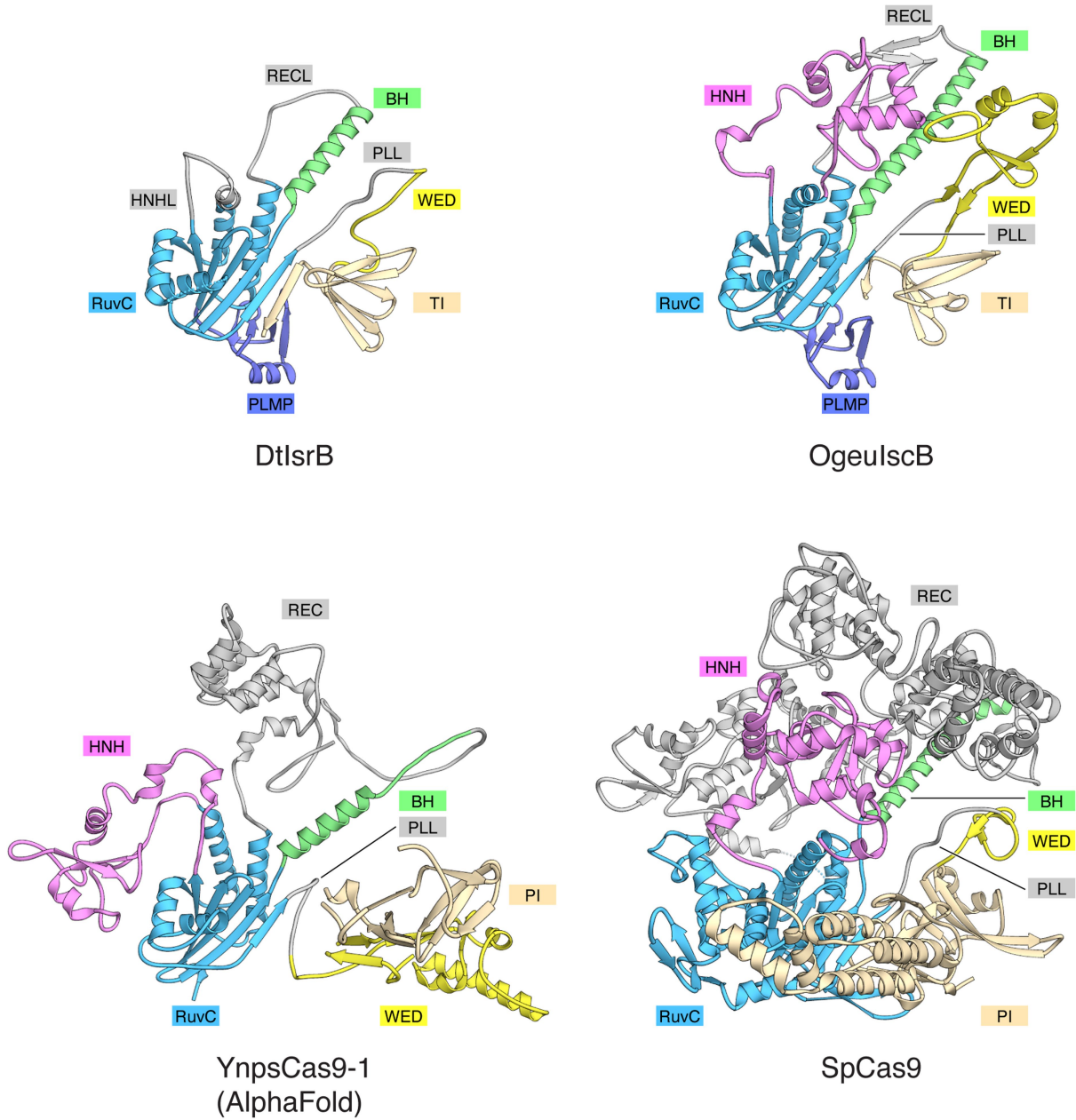
(a) Cleavage sites in the target DNA as assay by Sanger sequencing. The nicking sites are marked by black triangles. The additional non-templated adenine is indicated by an asterisk in the Sanger sequencing trace. (b) Domain structure of the λ N-IsrB fusion protein (left) and schematic of the ω RNA mutant and target DNA (right). In the ω RNA mutant, residues 34–67 were replaced with GAAA and boxB RNA was appended to the 3' end of the ω RNA scaffold. (c) Cryo-EM data processing schematic for single particle analysis of complex B (Left). Final refined map (Right). (d) FSC curves

calculated between the half maps of complex B from the final round of the refinement in cryoSPARC v3.3. (e) Cryo-EM density map of complex B. Based on the superposition of complex B map and complex A model, regions of protein, RNA, and DNA were assigned. Extra density was observed in the vicinity of the ω RNA SL8 region and assigned to the λ N-boxB complex, consistent with the SL8-boxB connectivity and the λ N-boxB volume (PDB: 1QFQ). TS, target strand; NTS, non-target strand. (f and g) Cryo-EM density maps of complex A (f) and SpCas9 in complex with its cognate RNA and target DNA (EMD: 24838) (g).

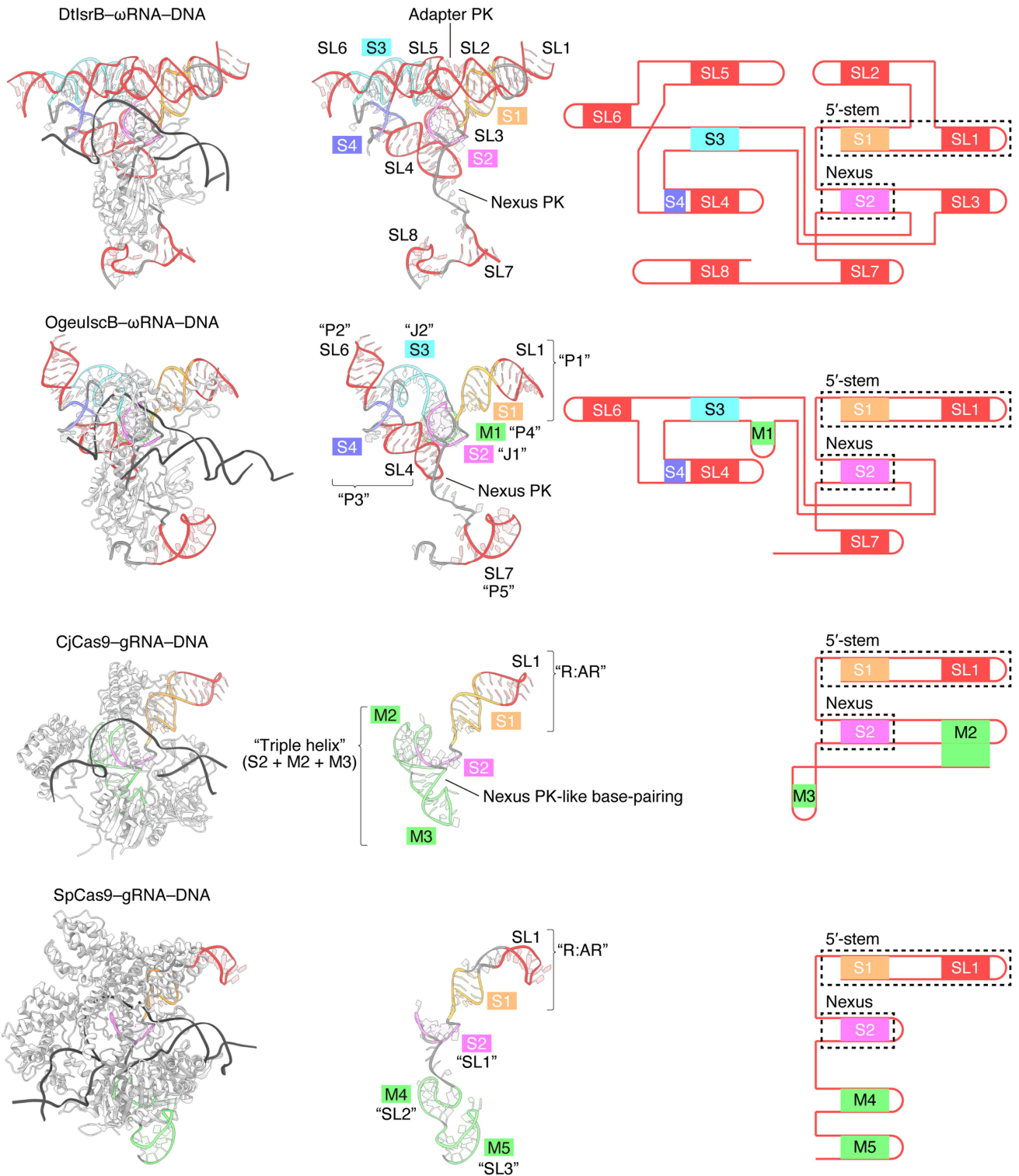


Extended Data Fig. 7 | Structural prediction of IsrB orthologs and their cognate ω RNAs. (a) Secondary structure and pseudoknot prediction of the ω RNA scaffolds based on covariance model. In CwIsrB/DsIsrB/BbIsrB ω RNAs, SL3 motifs are replaced with unpaired nucleotides. In CsIsrB/K2IsrB/BbIsrB ω RNAs, SL6 motifs are degenerated and SL8 motifs are replaced with unpaired

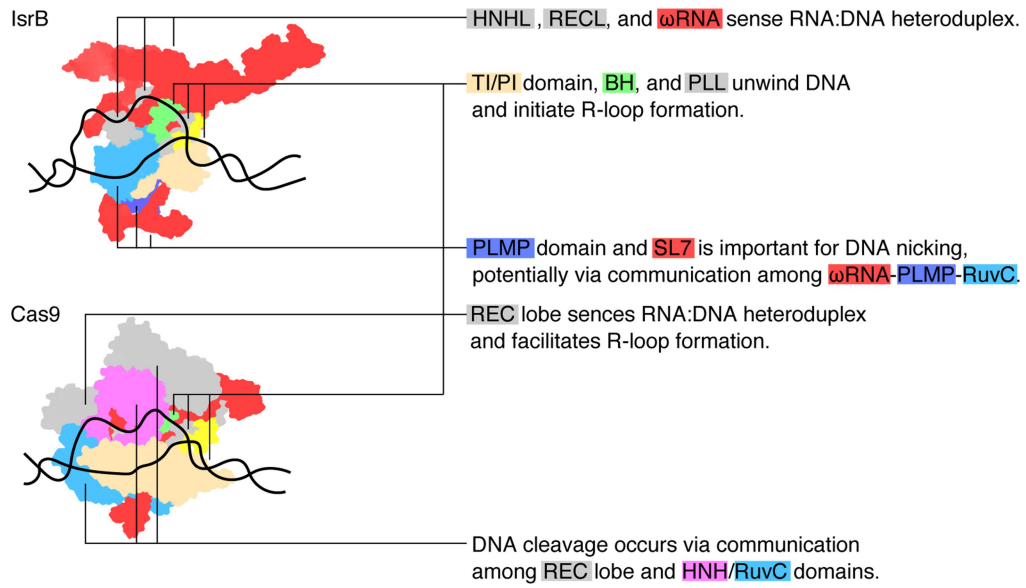
nucleotides. (b) Superposition of AlphaFold (AF) and cryo-EM (EM) structures of DtIsrB. (c) Superposition of AlphaFold structures of six IsrB orthologs. CwIsrB/DsIsrB have β -hairpin and loop insertions in the RuvC domain and RECL, respectively.



Extended Data Fig. 8 | Evolutionary snapshot of Cas9 ancestors. Structural comparison between DtlSrB, OgeulscB (8CSZ), YnpsCas9-1 (AF2 model), and SpCas9 (PDB: 4O08).



Extended Data Fig. 9 | Evolutionary snapshot of tracrRNA ancestors. Structural comparison between cognate RNAs of DtlrB, OgeulscB (8CSZ), CjCas9 (5X2G), and SpCas9 (7S4X) in their protein/DNA-bound states. Overall structures (left). RNA structures (center). RNA schematic diagrams (right).



Extended Data Fig. 10 | Models of RNA-guided DNA nicking/cleavage by IsrB/Cas9. Schematic highlighting the mechanistic similarities and differences between IsrB and Cas9.

Extended Data Table 1 | Cryo-EM data collection, refinement, and validation statistics

	Complex A (EMDB-27533) (PDB 8DMB)	Complex B (EMDB-26723)
Data collection and processing		
Magnification	105,000	120,000
Voltage (kV)	300	200
Electron exposure (e ⁻ /Å ²)	60	62.53
Defocus range (μm)	-2.2 to -0.8	-2.6 to -1.0
Pixel size (Å)	0.839	1.255
Symmetry imposed	C1	C1
Initial particle images (no.)	1,626,574	1,595,000
Final particle images (no.)	58,188	50,661
Map resolution (Å)	3.1	6.9
FSC threshold: 0.143		
Map resolution range (Å)	3.1 to 8.9	6.0 to 13.8
Refinement		
		N/A
Initial model used (PDB code)	N/A	
Model resolution (Å)	3.2	
FSC threshold: 0.5		
Map sharpening <i>B</i> factor (Å ²)	-73.1	
Model composition		
Non-hydrogen atoms	8497	
Protein residues	328	
Nucleotide residues	275	
Ligands	2	
<i>B</i> factors (Å²)		
Protein	24.60	
Nucleotide	62.18	
Ligand	21.56	
R.m.s. deviations		
Bond lengths (Å)	0.005	
Bond angles (°)	0.902	
Validation		
MolProbity score	0.86	
Clashscore	0.87	
Poor rotamers (%)	0.74	
Ramachandran plot		
Favored (%)	97.53	
Allowed (%)	2.47	
Disallowed (%)	0.00	

Reporting Summary

Nature Portfolio wishes to improve the reproducibility of the work that we publish. This form provides structure for consistency and transparency in reporting. For further information on Nature Portfolio policies, see our [Editorial Policies](#) and the [Editorial Policy Checklist](#).

Statistics

For all statistical analyses, confirm that the following items are present in the figure legend, table legend, main text, or Methods section.

n/a Confirmed

- The exact sample size (n) for each experimental group/condition, given as a discrete number and unit of measurement
- A statement on whether measurements were taken from distinct samples or whether the same sample was measured repeatedly
- The statistical test(s) used AND whether they are one- or two-sided
Only common tests should be described solely by name; describe more complex techniques in the Methods section.
- A description of all covariates tested
- A description of any assumptions or corrections, such as tests of normality and adjustment for multiple comparisons
- A full description of the statistical parameters including central tendency (e.g. means) or other basic estimates (e.g. regression coefficient) AND variation (e.g. standard deviation) or associated estimates of uncertainty (e.g. confidence intervals)
- For null hypothesis testing, the test statistic (e.g. F , t , r) with confidence intervals, effect sizes, degrees of freedom and P value noted
Give P values as exact values whenever suitable.
- For Bayesian analysis, information on the choice of priors and Markov chain Monte Carlo settings
- For hierarchical and complex designs, identification of the appropriate level for tests and full reporting of outcomes
- Estimates of effect sizes (e.g. Cohen's d , Pearson's r), indicating how they were calculated

Our web collection on [statistics for biologists](#) contains articles on many of the points above.

Software and code

Policy information about [availability of computer code](#)

Data collection

Data analysis

For manuscripts utilizing custom algorithms or software that are central to the research but not yet described in published literature, software must be made available to editors and reviewers. We strongly encourage code deposition in a community repository (e.g. GitHub). See the Nature Portfolio [guidelines for submitting code & software](#) for further information.

Data

Policy information about [availability of data](#)

All manuscripts must include a [data availability statement](#). This statement should provide the following information, where applicable:

- Accession codes, unique identifiers, or web links for publicly available datasets
- A description of any restrictions on data availability
- For clinical datasets or third party data, please ensure that the statement adheres to our [policy](#)

Human research participants

Policy information about [studies involving human research participants and Sex and Gender in Research](#).

Reporting on sex and gender	<input type="text" value="NA. Human research participants are not involved in this study."/>
Population characteristics	<input type="text" value="NA. Human research participants are not involved in this study."/>
Recruitment	<input type="text" value="NA. Human research participants are not involved in this study."/>
Ethics oversight	<input type="text" value="NA. Human research participants are not involved in this study."/>

Note that full information on the approval of the study protocol must also be provided in the manuscript.

Field-specific reporting

Please select the one below that is the best fit for your research. If you are not sure, read the appropriate sections before making your selection.

Life sciences Behavioural & social sciences Ecological, evolutionary & environmental sciences

For a reference copy of the document with all sections, see nature.com/documents/nr-reporting-summary-flat.pdf

Life sciences study design

All studies must disclose on these points even when the disclosure is negative.

Sample size	<input type="text" value="For complex A/B data analyses, 4142/2542 micrographs and 58188/50661 final particle images are used, respectively."/>
Data exclusions	<input type="text" value="To obtain the higher resolution image of cryo-EM reconstitution, the damaged and 'bad' particles are excluded, based on the software algorithm of single-particle analysis."/>
Replication	<input type="text" value="Cryo-EM data processing methods used in RELION and cryoSPARC softwares are well-established and reproducible. DNA nicking experiments are repeated at least three times and confirmed for their reproducibility."/>
Randomization	<input type="text" value="NA"/>
Blinding	<input type="text" value="NA"/>

Reporting for specific materials, systems and methods

We require information from authors about some types of materials, experimental systems and methods used in many studies. Here, indicate whether each material, system or method listed is relevant to your study. If you are not sure if a list item applies to your research, read the appropriate section before selecting a response.

Materials & experimental systems

n/a	Involvement in the study
<input checked="" type="checkbox"/>	<input type="checkbox"/> Antibodies
<input checked="" type="checkbox"/>	<input type="checkbox"/> Eukaryotic cell lines
<input checked="" type="checkbox"/>	<input type="checkbox"/> Palaeontology and archaeology
<input checked="" type="checkbox"/>	<input type="checkbox"/> Animals and other organisms
<input checked="" type="checkbox"/>	<input type="checkbox"/> Clinical data
<input checked="" type="checkbox"/>	<input type="checkbox"/> Dual use research of concern

Methods

n/a	Involvement in the study
<input checked="" type="checkbox"/>	<input type="checkbox"/> ChIP-seq
<input checked="" type="checkbox"/>	<input type="checkbox"/> Flow cytometry
<input checked="" type="checkbox"/>	<input type="checkbox"/> MRI-based neuroimaging